Journal of Geochemical Exploration 163 (2016) 53–69

Contents lists available at ScienceDirect

Journal of Geochemical Exploration

journal homepage: www.elsevier.com/locate/gexplo

Influences of fluid properties on the hydrothermal fluid flow and alteration halos at the Dajishan tungsten deposit, China

Xiangchong Liu [a,b], Huilin Xing [c], Dehui Zhang [b,*]

[a] Institute of Geomechanics, Chinese Academy of Geological Sciences, Beijing 100081, China
[b] State Key Laboratory of Geological Processes and Mineral Resources, School of Earth Sciences and Resources, China University of Geosciences (Beijing), Beijing 100083, China
[c] Centre for Geoscience Computing, School of Earth Sciences, The University of Queensland, Brisbane, QLD 4072, Australia

ARTICLE INFO

Article history:
Received 19 May 2015
Revised 14 December 2015
Accepted 19 January 2016
Available online 21 January 2016

Keywords:
Dajishan
Tungsten
Alteration halo
Viscosity
Effective diffusion
Porosity

ABSTRACT

The Nanling Range located in South China is a world-class tungsten province. Those tungsten deposits are spatially and temporally associated with the granitic magmatism during the Late Mesozoic (J_2-K_2). It is common that alteration halos decrease with increasing depth at the vein-type tungsten deposits. However, the mechanisms forming the alteration characteristics are still enigmatic. In this contribution, we investigate the influences of variable fluid density and viscosity on the fluid flow and species diffusion from fractures to adjacent wallrock at the Dajishan tungsten deposit using finite element based numerical experiments. Fluid density has a negative influence on the transient pressure-driven fluid flow at Dajishan. Large-density fluids slow fluid flow and heat transfer. High-viscosity fluids flow slowly. Variations of fluid viscosity at Dajishan are large and influence hydrothermal fluid flow and species diffusion from fractures to surrounding wallrock. Depth-dependent porosity and permeability of wallrock are effective mechanisms forming the alteration halos at Dajishan. Hydraulic and geometric characteristics of joint zones influence diffusion of chemical species at the initial stages of hydrothermal fluids injected into fractures. High-permeability narrow joint zones favor formation of thick alteration halos at shallower levels. Depth-dependent wallrock porosity also impedes diffusion of metals from fractures to adjacent wallrock increasing ore formation efficiency at Dajishan.

1. Introduction

The Nanling Range is a world-class tungsten province in China (Mao et al., 2013). Tungsten deposits in this area have a close spatial and temporal relationship to granitic magmatism during the Late Mesozoic (J_2-K_2) (Mao et al., 2013; Zhou et al., 2006). The veins at those tungsten deposits are often subvertical and have narrow zones of wallrock alteration, which is independent of the wallrock types (Chen et al., 1989; Liu and Ma, 1993; Wei et al., 2012; Zhu et al., 1981). Moreover, the wallrock alteration is weaker at the deeper levels, which is closer to the source to the hydrothermal fluids (Chen et al., 1989). A view of the alteration characteristics is that the magmatic-hydrothermal fluids are between silicates and aqueous solutions and have variable physical properties (Chang et al., 2006; Chen et al., 1989; Lin et al., 1986; Zhang, 1987; Zhu et al., 2014, 1981). However, existing fluid inclusion data suggest that the mineralized fluids are aqueous NaCl solutions (e.g. Cao et al., 2009; Gong et al., 2015; Liu et al., 2011; Ni et al., 2015; Wang et al., 2013b; Wei et al., 2012). The formation of magmatic-hydrothermal deposits involves complicated fluid flow mechanisms and processes (e.g. Hayba and Ingebritsen, 1997; Ingebritsen and Appold, 2012; Ingebritsen et al., 2010). Previous studies have focused on the geochemical behaviors of magmatic-hydrothermal fluids at the tungsten deposits in this area (e.g. Chang et al., 2006; Chen et al., 1989; Hu et al., 2012; Wang et al., 2003; Wei et al., 2012; Yang et al., 2013; Zhu et al., 2014); however, it is poorly understood how the physical properties of magmatic-hydrothermal fluids influence the fluid flow and mineralization.

Two fluid physical parameters are present in Darcy's equation that controls the fluid flow in porous media, fluid density and viscosity (Phillips, 1991). Fluid density is related to gravity, which is a component of the force driving fluid flow in rocks (Chi and Xue, 2011; Hubbert, 1953). Fluid density differences produce buoyancy influencing the flow strength and direction (Bachu, 1995; Hack et al., 2007). However, previous studies on porphyry copper deposits suggest that the buoyancy-driven convective flow controlled by fluid density is suppressed by pressure-driven flow when magmatic-hydrothermal fluids are released from a fluid-saturated magma (e.g. Gerdes et al., 1998; Hanson, 1995; Weis, 2015). It is unclear whether such a conclusion from porphyry copper deposits is applicable at the tungsten deposits in the Nanling Range.

Fluid viscosity is a parameter influencing fluid velocity for a given driving force and diffusion of chemical species in aqueous solutions

* Corresponding author at: State Key Laboratory of Geological Processes and Mineral Resources, School of Earth Sciences and Resources, China; University of Geosciences (Beijing), Beijing 100083, China.
E-mail addresses: xcliu@cags.ac.cn (X. Liu), h.xing@uq.edu.au (H. Xing), zhdehui@cugb.edu.cn (D. Zhang).

http://dx.doi.org/10.1016/j.gexplo.2016.01.014
0375-6742/

(Adams and Bachu, 2002; Li and Gregory, 1974). A few empirical formulas derived by fitting laboratory data suggest that the viscosity of basin brines varies by one order of magnitude (Adams and Bachu, 2002). Moreover, silicate-rich aqueous fluid inclusions or silicate melts coexisting with aqueous fluids are found in some ore-related granites and pegmatites (e.g. Davidson and Kamenetsky, 2001; Kamenetsky et al., 1999; Thomas and Davidson, 2012; Thomas et al., 2000; Veksler, 2004). The viscosity of silicate-bearing aqueous fluids varies several orders of magnitude (Audétat and Keppler, 2004). Therefore, it is necessary to examine the influences of fluid density and viscosity variations on fluid flow at magmatic-hydrothermal conditions.

In this contribution, we investigate how temperature- and pressure-dependent fluid density and viscosity influence the fluid flow and alteration halos at the Dajishan tungsten deposit using finite element based numerical experiments. We find that fluid density has a negative influence on pressure-driven flow and fluid viscosity affects fluid flow and fluid-wallrock alterations significantly at the temperature and pressure ranges of the deposit. Depth-dependent porosity and permeability of the wallrock are effective mechanisms forming the alteration characteristics at Dajishan.

2. Geological background

The Dajishan tungsten deposit is a granite- and vein-type tungsten polymetallic deposit in the Nanling Range, South China (Fig. 1). The mineralized granite is locally called the Number 69 Muscovite Granite. The vein-type deposit has a total of approximately 160,000 tonnes of WO_3 with an average grade of 2.04% (Mao et al., 2013).

The granites at Dajishan include biotite granite, two-mica granite, and muscovite granite (Fig. 1). The Wuliting biotite granite is exposed in the north of the deposit and has an exposed area of approximately 100 km^2 (Zhou, 2009). The granite is composed mainly of plagioclase, microcline, biotite, quartz, and allanite (Zhuang et al., 1991). The contact relationship between the biotite granite and the other granites is unknown. The zircon U–Pb ages of the biotite granite are 238.4 ± 1 Ma and 237.5 ± 4.8 Ma (Qiu et al., 2004; Zhang et al., 2004), whereas its whole-rock Rb–Sr age is 167 ± 1 Ma and its biotite K–Ar ages are 160.3 ± 3.0 Ma and 164.2 ± 3.5 Ma (Jiang et al., 2004; Sun, 1989).

The medium-grained two-mica granite is present below the 240 m level and consists of plagioclase, K-feldspar, perthite, quartz, muscovite, and biotite (Zhuang et al., 1991). The veins are present above this granite. The two-mica granite has a whole-rock Rb–Sr age of 161 Ma and a muscovite K–Ar age of 160.6 ± 2.8 Ma (Jiang et al., 2004; Sun, 1989).

The muscovite granite is present from the 517 m to 0 m levels and consists of five small intrusions, the largest one of which is Ta–Nb–W–Be mineralized and locally called the Number 69 Granite. Major rock-forming minerals of the muscovite granite include microcline, albite, quartz, muscovite, columbite–tantalite, wolframite, sheellite, Nb-aeschynite (Zhuang et al., 1991). The Number 69 Granite is sickle-shaped and has an area of approximately 0.04 km^2. The contact relation suggests that the muscovite granite is emplaced later than the two-mica granite but earlier than the veins (Zhou, 2009). The Number 69 Granite has a whole-rock Rb–Sr age of 159 ± 5 Ma and a zircon U–Pb age of 151.7 ± 1.6 Ma (Sun, 1989; Zhang et al., 2006).

The muscovite granite has two textural zones: a marginal pegmatite zone and a fine-grained zone (Fig. 2). The pegmatitic unit or stockscheider has a sharp contact relation to the wallrock and is composed of coarse-grained microcline and quartz (Lu et al., 1974). The stockscheider is a few cm to 1 m thick, reaching the maxima at the horizontal contact. The grain size of the microcline varies from 5 to 10 cm.

The two-mica and muscovite granites are enriched with respect to Si, Na, Mn, HREE and are depleted with respect to Ti, Fe, Mg, Ca, LREE compared to the biotite granite (Lu et al., 1974; Qiu et al., 2004; Sun, 1989). The stockscheider is enriched with respect to Si and K compared to the fine-grained muscovite granite (Lu et al., 1974). Previous geochemical studies suggest that the two-mica and muscovite granites have a closer relationship to the mineralization than the biotite granite (Qiu et al., 2004; Sun, 1989).

The mineralization in the veins has a molybdenite Re–Os age of 160 ± 1 Ma (Zhang et al., 2011), muscovite K–Ar ages of 152.2 ± 2.4 Ma and 158.1 ± 2.8 Ma (Jiang et al., 2004), and muscovite ^{40}Ar–^{39}Ar ages of 147 and 144 Ma (Zhang et al., 2006). Hydrogen, oxygen, carbon, and sulfur isotopic data indicate that the ore fluids have a magmatic origin at the main mineralization stage, and then are mixed with meteoric waters at late stages (Sun, 1989; Zhang et al., 1997; Zhuang et al., 1991).

The ore fluids are in NaCl–H_2O ± CO_2 systems (Ni et al., 2015; Wang et al., 2013a; Xi et al., 2008). The fluid inclusions at room temperature are mainly two-phase aqueous-rich. The fluid inclusions in wolframite have a homogenization temperature range from 240° to 369 °C, whereas the homogenization temperatures of fluid inclusions in quartz vary from 176° to 325 °C (Ni et al., 2015; Wang et al., 2013a; Xi et al., 2008). The fluid inclusions in wolframite have salinities from 4.3 to 9.0 wt.% NaCl equivalent, and those in quartz range from 0.2 to 12 wt.% NaCl equivalent (Ni et al., 2015; Wang et al., 2013a; Xi et al., 2008). Some aqueous-carbonic inclusions in quartz are trapped under

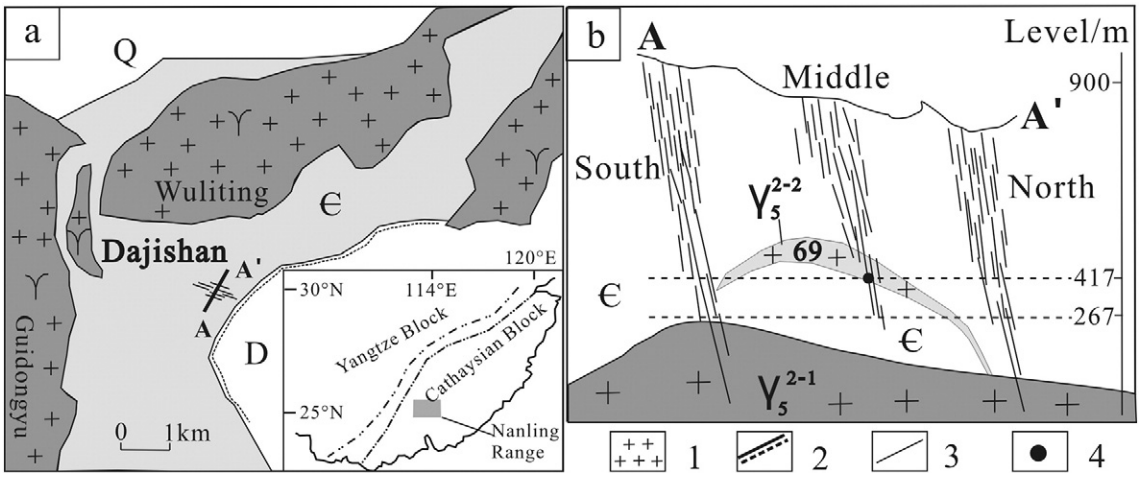

Fig. 1. (a) A regional geological map of the Dajishan tungsten deposit, revised from Sun (1989) and Yang et al., (2009); (b) A cross section of the Dajishan deposit along the line A–A', revised from Sun (1989). 69 is the Number 69 Muscovite Granite. 1, granite; 2, unconformity; 3, tungsten-bearing quartz veins; 4, the locations of the stockscheider and the feldspar-quartz veins. γ, granite; γ_5^{2-1}, two-mica granite; γ_5^{2-2}, muscovite granite; Q, Quaternary; D, Devonian; Є, Cambrian.

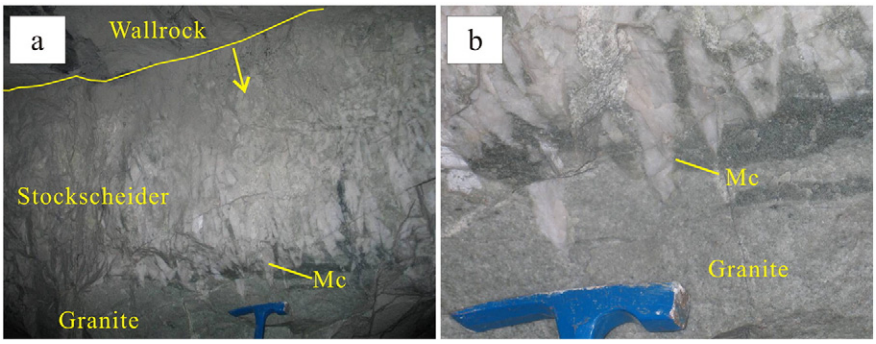

Fig. 2. The stockscheider in the margin of the muscovite granite at Dajishan. (a) The stockscheider shows a sharp contact with the fine-grained muscovite granite at 417 m level. View to upwards. (b) A closer view of the photo (a) showing the coarse-grained microcline inserted into the granite. Abbreviations: Mc, microcline; Granite, fine-grained muscovite granite.

fluid immiscibility, and the trapping pressures are from 114 MPa to 132 MPa (Xi et al., 2008).

3. Alteration halos at Dajishan

The veins at Dajishan are parallel and subvertical. These veins are divided into three vein sets based on their locations and mineral assemblages: the north, the middle, and the south vein sets (Fig. 1). The average thickness of veins increases downwards from less than 1 cm thick at 985 m level to 0.2 m below 467 m level with the maximum reaching 2 m (Liu et al., 2014). Ore minerals in the veins include wolframite, scheelite, tungstite, bismuthinite, native Bi, and molybdenite, and gangue minerals have quartz, feldspar, muscovite, calcite, and tourmaline (Zhou, 2009).

Most veins in the middle vein set are present in diorite and the veins in the north and south vein sets are present at the metamorphosed Cambrian sandstone. Alteration is generally confined to the vein fringes and characterized by the mineral assemblage of silica-pyrite-biotite-muscovite in sandstone and the mineral assemblage of pyrite–tourmaline–chlorite–epidote in diorite (Que and Xia, 1988; Sun, 1989). Previous studies indicate that the alteration halos are thicker at shallower levels than those at deeper levels, which is independent on the specific alteration and wallrock lithology (Que and Xia, 1988). Note that the veins are intensively mineralized at deeper levels, whereas the veins at shallower levels are barren (Que and Xia, 1988). Fig. 3 shows the sharp contact between a thick vein and weakly altered sandstone.

Alteration halos are produced after a volume of reactive fluids injected into fractures alters the surrounding rocks (cf. Cathles and Shannon, 2007). Alteration halo width depends on the physical and chemical properties of fluids and rocks, the diffusion rate, and the duration (e.g. Cathles and Shannon, 2007; Geiger et al., 2002; Steefel and Lichtner, 1998). Neither alteration in sandstone nor in diorite varies significantly at the different levels at Dajishan. Therefore, it seems inappropriate to attribute the physical properties of the wallrock to the alteration feature at Dajishan. When the physical and chemical properties of fluids and rocks are constant, alteration halo width decreases as reactive fluids flow away from the source (Cathles and Shannon, 2007; Steefel and Lichtner, 1998). Moreover, the reverse zonation of the mineral assemblages at Dajishan suggests that the late-stage ore fluids flowed only at deeper levels. Thus, it is problematic to attribute the flow duration to the different alteration halo width.

Fluid properties and diffusion rate are left to be potential factors influencing the alteration halos at Dajishan. Que and Xia (1988) envisage that the ore fluids may be silica-rich and have a relatively high density and viscosity. An important basis for this is that feldspar-quartz veins are present at deeper levels of the middle vein set (Fig. 4). Feldspar aggregates in these veins are massive and often contain orthoclase, microcline, and plagioclase (Zhou, 2009). The contact relation between quartz and feldspar is different from the graphic intergrowth in granitic pegmatite (e.g. London, 2014). The problem of Que. and Xia's point is that melt inclusions have not been found neither in the feldspar-quartz veins and nor in the stockscheider (Lu et al., 1974; Ma and Chen, 1984). Moreover, the feldspar–quartz veins are absent in the north and south vein sets. Therefore, the alteration characteristics at Dajishan may not be related to the silica-rich fluids. Diffusion rate of chemical species is controlled by the diffusion coefficient and concentration gradient according to Fick's first law (Li and Gregory, 1974). The diffusion coefficient of chemical species in aqueous solutions depends on fluid viscosity and temperature (Li and Gregory, 1974). Therefore, it is necessary to re-examine how fluid properties influence the fluid flow and fluid-wallrock interaction at Dajishan as temperature and pressure change.

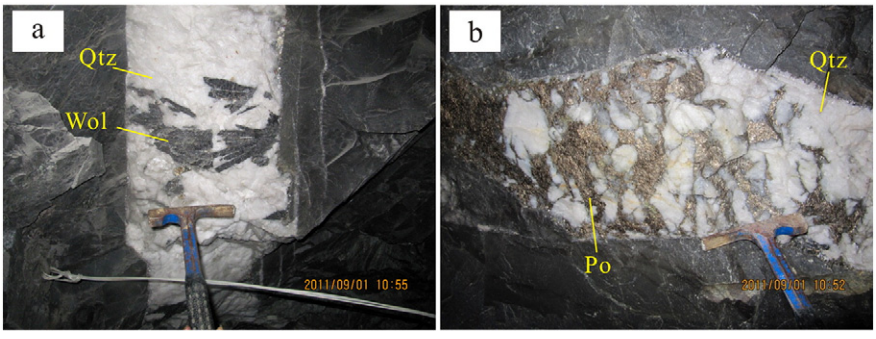

Fig. 3. Photos of the mineral assemblages at the Dajishan deposit. (a) Tabular wolframite is present perpendicular to the vein walls at 417 m level (Liu et al., 2014). View to upwards. (b) The early quartz is enveloped by the late pyrrhotite in a thick vein at 417 m. View to upwards. Abbreviations: Po, pyrrhotite; Qtz, quartz; Wol, wolframite.

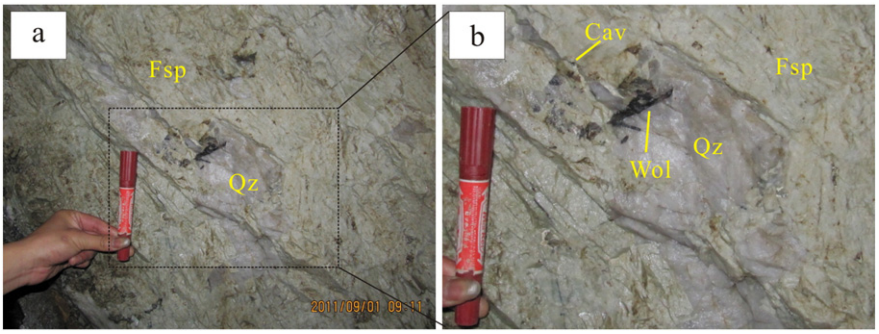

Fig. 4. Photos of the feldspar-quartz veins in the middle vein set at Dajishan. (a) A segment of the locally called the Number 6 Vein at 417 m level. The vein segment contains over 90% feldspar, massive quartz, and tabular wolframite. View to NWW. (b) A closer view of the photo (a) showing the contact relation between irregular quartz and tabular feldspar. There is also a small cavity adjacent to the contact between quartz and feldspar. Abbreviations: Cavity, cavity; Fsp, feldspar; Qtz, quartz; Wol, wolframite.

4. Numerical modeling at Dajishan

4.1. Mathematical theories

The simulation tool we used is called PANDAS (Parallel Adaptive Nonlinear Deformation Analysis Software), which is an in-house finite element based supercomputer simulator. The developers and users of PANDAS have made much progress in understanding the coupled hydraulic–thermal–mechanical behaviors in fault systems, ore forming processes, and geothermal reservoirs (Li and Xing, 2015; Xing, 2014; Xing et al., 2015, 2007; Xing and Makinouchi, 2002). This simulator was employed to investigate the hydrothermal fluid flow at Dajishan.

The simultaneous partial differential equations solved by PANDAS include continuity equation and Darcy's equation (Xing, 2014). An equivalent continuous medium was used in this paper (e.g. Oda, 1985). For the conservation of non-deformable rock mass with a constant porosity ϕ, the continuity equation is expressed as:

$$\phi\beta_m \frac{\partial P}{\partial t} + \nabla\cdot(\rho \boldsymbol{\nu}) = 0 \tag{1}$$

where β_m is the effective compressibility, P is the fluid pressure, ρ is the fluid density, and $\boldsymbol{\nu}$ is the fluid velocity. $\beta_m = \phi\beta_f + \beta_r(1-\phi)$, where β_f, β_r are the compressibility of fluid and rock matrix, respectively. The bold symbols are used for vectors, tensors, and matrix variables throughout this paper.

Groundwater flow in porous media is commonly assumed to follow Darcy's law (Phillips, 1991). In this study, the fluid flow follows Darcy's equation (Xing, 2014):

$$\boldsymbol{\nu} = -\frac{\boldsymbol{k}}{\mu(}(\nabla P - \rho \boldsymbol{g}\nabla \boldsymbol{D}) \tag{2}$$

where $\boldsymbol{k}$ is the intrinsic permeability tensor of the porous media, μ is the dynamic viscosity, $\boldsymbol{g}$ is the gravitational acceleration, and $\boldsymbol{D}$ is the depth.

The conductive-convective heat transfer in porous media is described as:

$$(\rho C)_m \frac{\partial T}{\partial t} = -\nabla\cdot(-\lambda_m \nabla T) - (\rho C)_f \boldsymbol{\nu}\cdot\nabla T + Q_e \tag{3}$$

where $(\rho C)_m = (1-\phi)(\rho C)_r + \phi(\rho C)_f$, ρ is density, C is specific heat capacity; heat conductivity $\lambda_m = \phi\lambda_f + (1-\phi)\lambda_r$; T is the temperature; Q_e is the energy source term. The subscripts r, f, and m denote rock matrix, fluid, and mixture, respectively (Xing, 2014).

NaCl–H_2O systems are liquid-phase at the temperature, pressure, and salinity ranges recorded by the fluid inclusions at Dajishan (c.f. Fournier, 1999). Both density and viscosity of aqueous NaCl solutions depend on temperature, pressure, and salinity (e.g. Adams and Bachu, 2002). The density model fitted by Batzle and Wang (1992) is accurate in wide temperature and pressure conditions (Adams and Bachu, 2002). Phillips et al. (1981) develop a good viscosity model for NaCl solutions. His viscosity model requires accurate viscosity of pure water. To save computational cost, we used the simplified water viscosity model developed by Mao and Duan (2009) (See Appendix A). The comparison between the numerical viscosity and experimental data in Pepinov et al. (1977) and Semenyuk et al. (1977) suggests that the viscosity model used in this paper is in agreement with the experimental data (Fig. 5). Therefore, the viscosity and density models above were incorporated into the simulator code. The fluid density and viscosity curves shown in Fig. 5 suggest that both density and viscosity depend mainly on temperature, and pressure has a minor influence on the two parameters.

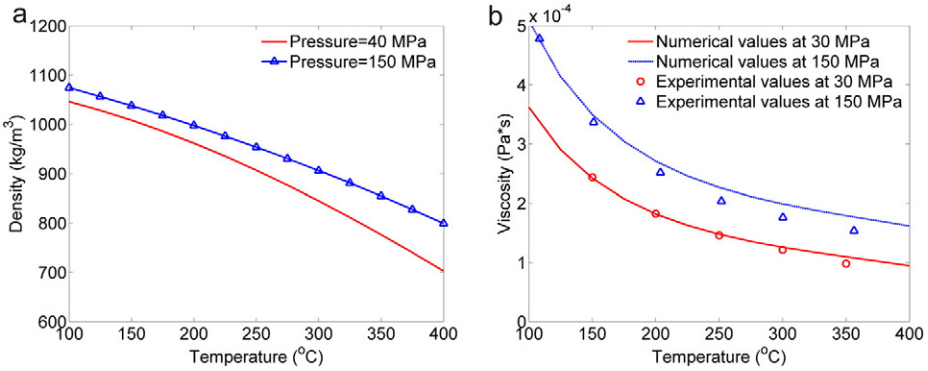

Fig. 5. Fluid density (a) and viscosity (b) derived from the functions used in this paper. The experiment data at 30 MPa and 150 are from Pepinov et al. (1977) and Semenyuk et al. (1977). The viscosity derived from the viscosity function in this paper is close to the experimental data. For the numerical and experiment data at 30 MPa, the fluid salinity is 10 wt.% NaCl equivalent. For the numerical and experiment data at 150 MPa, the fluid salinity is 19.12 wt.% NaCl equivalent.

The Péclet number is a dimensionless number characterizing the ratio of advective transport rate to diffusive transport rate (Lester et al., 2012):

$$Pe = \frac{L|\boldsymbol{\nu}|}{D_e} \tag{4}$$

where L is the fracture aperture, $\boldsymbol{\nu}$ is the flow velocity, and D_e is the effective diffusion coefficient of chemical species in porous media. Pe > 1 means that advection dominates over diffusion; otherwise, diffusion prevails over advection. Chemical reactions are dominated by reaction–diffusion processes when Pe < 1 (Lester et al., 2012). The effective diffusion coefficient of chemical species in porous media is a function of the porosity ϕ and the diffusion coefficient D_s in aqueous solutions:

$$D_e = D_s\phi^n \tag{5}$$

where n is a constant ranging from 2 to 3 (e.g. Boving and Grathwohl, 2001; Van Loon and Mibus, 2015). For rocks with a porosity of less than 0.1, the constant n approaches the lower bound 2; for rocks with a higher porosity, the constant may reach its upper bound 3 (Van Loon and Mibus, 2015). The cubic law links the fracture aperture to the permeability in Eq. (2) (Oda, 1985; Snow, 1969).

Findings from porphyry systems suggest that formation of alteration halos is at time scales of decades and hundred years (e.g. Cathles and Shannon, 2007; Geiger et al., 2002). A function proposed by Cathles and Shannon (2007) was used to quantify the alteration halo width normal to veins:

$$Z(t) = \sqrt{\frac{2D_e t}{G}} \tag{6}$$

where Z is the width of alteration halos formed during the time t and G is a dimensionless parameter that equals the volume (m^3) of fluid required to alter 1 m^3 rock.

4.2. Model assumptions

The following simplifications were made to investigate transient flow at reasonable computational cost. First, high-pressure fluids were accumulated at the contact zone between fluid-saturated magma and host rock at Dajishan. This treatment was based on the close relationship between the granite and tungsten mineralization at Dajishan (see Section 2). Second, the numerical experiments were run for a short period of time. Findings from previous studies suggest that the fluid flow in fractured rocks is significantly influenced by the competition between permeability creation processes and permeability destruction processes in hydrothermal systems (e.g. Cann et al., 2015; Cox et al., 2001; Ingebritsen and Manning, 2010; Rutqvist, 2015; Stober and Bucher, 2015; Weis, 2015). Thus, the second treatment was made to mimic the transient flow without the influences of other physical and chemical processes. Third, the fluid flow was driven by a constant fluid pressure. This treatment was based on the high pressure recorded in the fluid inclusions at Dajishan. It is plausible to fix the driving pressure for a short geological time.

4.3. A 2-D numerical model at Dajishan

A 2-D numerical model was established by the geological and structural characteristics at Dajishan (Fig. 6). Z axis is vertical and X axis is in an orientation of NNE, which is normal to the veins. The size of the model is 2.0 km × 1.6 km. The model is at a depth from 4.0 km to 5.6 km, which is calculated from the trapping pressure of fluid inclusions and the lithostatic pressure gradient of 27 MPa/km (Xi et al., 2008).

The model has four units. Є1 is the contact zone between the crystallized granite and host rock. Є2 is the wallrock. J1 and J2 are the joint zones where the veins are present now. Only one vein set was considered in the model. Abundant joints are present close to the veins at Dajishan. Our previous studies suggest that the preferred oriented joints are parallel to the veins and potential conduits for mineralized fluids (Liu et al., 2014). Both vein and joint densities decrease downwards (Liu et al., 2014). The vein set width is approximately 60 m at shallower levels but decreases to 20–30 m at 267 m level. Thus, the joint zones are ladder-shaped in the model. The lower and upper bases are 20 m and 40 m, respectively. J1 has a height of 400 m and J2 has a height of 600 m. Two profiles are used to characterize the fluid flow in the joint zones and surrounding wallrock. One profile is at a depth of 5.4 km and the other is at a depth of 4.6 km. The model was discretized into 25,200 elements and 38,613 nodes.

4.4. Model parameters

We focused on the transient flow after the joint zones have higher permeability than the surrounding wallrock. Both J1 and J2 have a porosity of 10% and a permeability of 1.0×10^{-12} m^2. The constant zone Є1 has a porosity of 0.4% and a permeability of 1.0×10^{-17} m^2. The permeability of the wallrock Є2 follows a depth-dependent function fitted by Ingebritsen and Manning (2010):

$$\log k \approx -11.5 - 3.2\log Z \tag{7}$$

where the permeability scalar k is in m^2 and the depth Z is in km. The permeability is assumed to have a cubic law relationship to the porosity (Walder and Nur, 1984):

$$\frac{k}{k_0} = \left(\frac{\phi}{\phi_0}\right)^3 \tag{8}$$

where k_0 and ϕ_0 are the reference permeability and porosity, respectively. $k_0 = 1.0 \times 10^{-16}$ m^2 and $\phi_0 = 0.01$ were used in the model.

The effective compressibility depends on the compressibility of rock and fluid. The fluid compressibility was fixed at 6.0×10^{-10} Pa^{-1} (c.f. Rogers and Pitzer, 1982). The average rock compressibility of sandstone

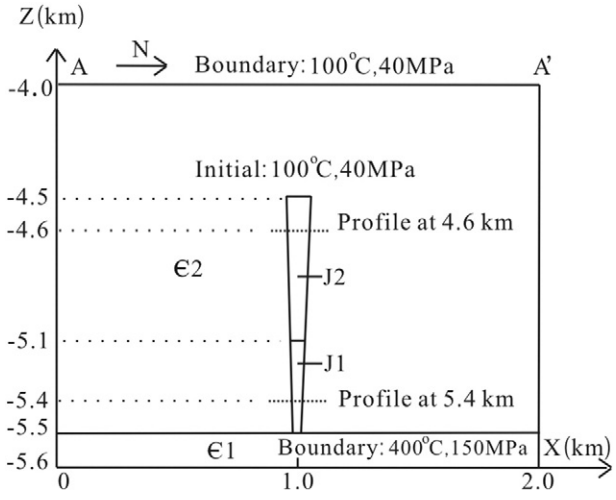

Fig. 6. The geometric model of the Dajishan tungsten deposit. The geometric model is 2.0 km × 1.6 km. X axis is perpendicular the veins at Dajishan. Z axis represents the depth. The model has four units, the contact zone Є1, the intact host rock Є2, the lower part of the joint zones J1, and the upper part of the joint zones J2. The two profiles cover the joint zones and adjacent wallrock. The initial and boundary conditions are described in Section 4.

Table 1
Key parameters and their variations in the six numerical experiments.

Experiments	Density	Viscosity	∈2 permeability (m^2)	J1,J2 permeability (m^2)	J1,J2 width (m)
E1	T–P-dependent		1.0×10^{-16}	1.0×10^{-12}	20
E2	Constant	T–P-dependent	1.0×10^{-16}	1.0×10^{-12}	20
E3	T–P-dependent	Constant	1.0×10^{-16}	1.0×10^{-12}	20
E4	T–P-dependent		Depth-dependent	1.0×10^{-12}	20
E5	T–P-dependent		Depth-dependent	2.0×10^{-12}	20
E6	T–P-dependent		Depth-dependent	2.0×10^{-12}	Ladder-shape

Other parameters not shown in this table are identical in the six numerical experiments.

at Dajishan is 2.8×10^{-11} Pa^{-1} (see Appendix B). Silification is the principle alteration at Dajishan. We used the diffusion coefficient of silica in aqueous solutions to calculate the Péclet number (see Appendix B).

The average density of wallrock at Dajishan is 2.8×10^3 kg/m^3 (Zhou, 2009). The specific heat capacity of rock and fluid are 1000 $J\cdot(kg\cdot K)^{-1}$ and 4200 $J\cdot(kg\cdot K)^{-1}$, respectively. The thermal conductivity of

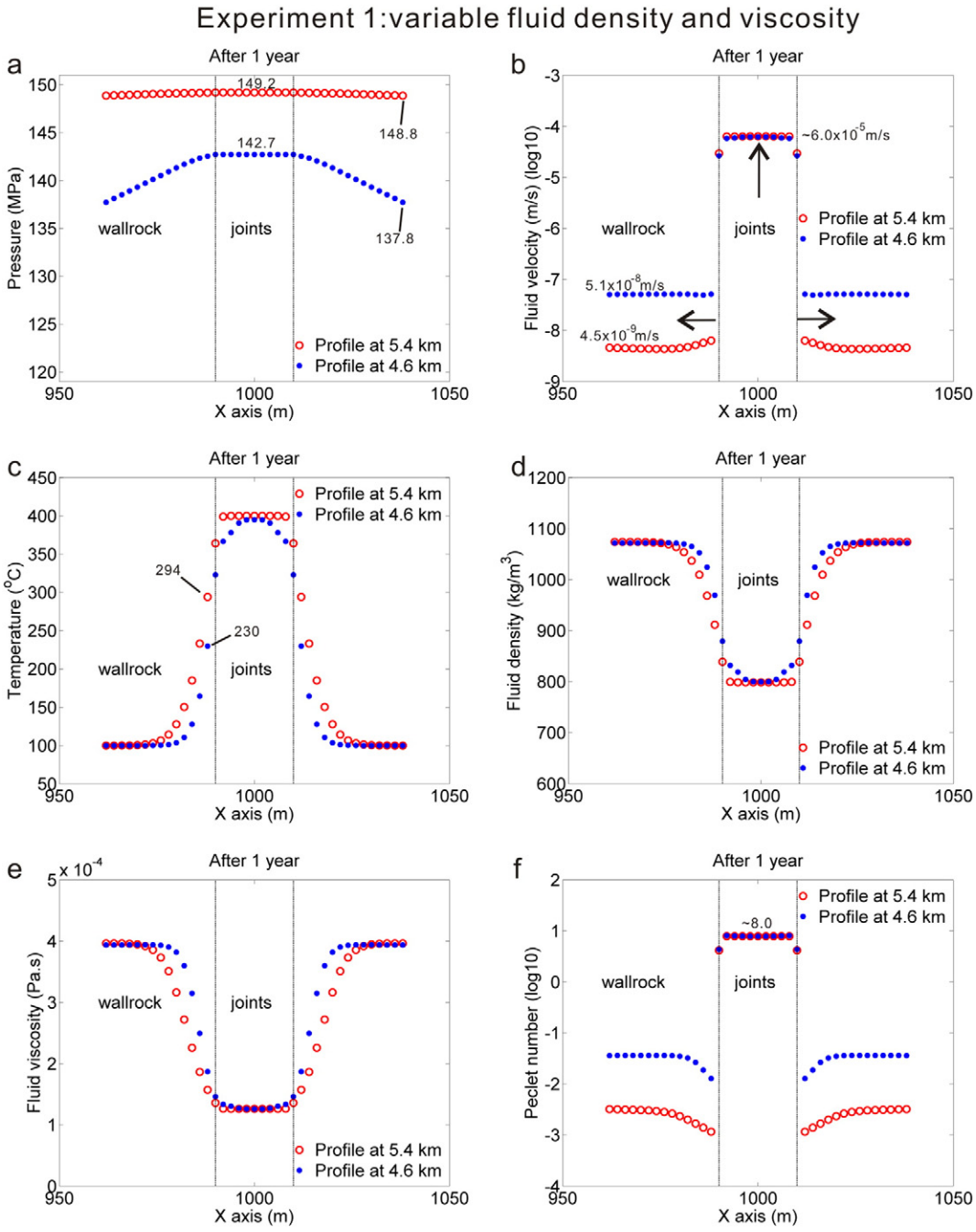

Fig. 7. The fluid flow and heat transfer in the two profiles in the first numerical experiment: (a), (b), (c), (d), (e) and (f) are the fluid pressure, velocity, temperature, fluid density, viscosity, and the Péclet number after 1 year, respectively. The temperature and Péclet number have been logarithmically transferred.

rock and fluid are 2.0 $W\cdot(m\cdot K)^{-1}$ and 0.6 $W\cdot(m\cdot K)^{-1}$, respectively (Bobertson, 1988).

The contact zone Є1 has a constant fluid pressure of 150 MPa and a constant temperature of 400 °C. The model top is fixed at a fluid pressure of 40 MPa and a temperature of 100 °C. The model has an initial fluid pressure of 40 MPa and an initial temperature of 100 °C. The fluid salinity is 10 wt.% NaCl equivalent.

5. Results

Six numerical experiments were conducted to investigate how fluid properties affected the hydrothermal flow and alteration halos at Dajishan. The key parameters and their variations in the six numerical experiments are listed in Table 1. The first numerical experiment (E1) is the reference experiment where the density and viscosity models were used. The next five experiments were designed to investigate the influences of fluid density, viscosity, depth-dependent permeability of wallrock, the hydraulic and geometric characteristics of joint zones, respectively. In the second numerical experiment (E2), fluid density is constant but viscosity is as variable as in E1. In the third numerical experiment (E3), fluid viscosity is constant but density is as variable as in E1. In the fourth numerical experiment (E4), the wallrock Є2 has a depth-dependent porosity and permeability compared to E1. In the fifth numerical experiment (E5), the joint zones J1 and J2 have higher porosity and permeability than those in E4. In the sixth numerical experiment (E6), the joint zones are ladder-shaped compared to E5. The results in the two profiles were output.

5.1. Numerical experiment with variable fluid density and viscosity

In the first numerical experiment, the fluid density and viscosity functions in Section 4.1 were used. The joint zones J1 and J2 have the same width and permeability and the contact zone (Є1) and the wallrock (Є2) has a constant porosity and permeability.

The fluid pressure in the profile at 5.4 km depth increased to higher levels (148.8–149.2 MPa) than that at 4.6 km depth (137.8–142.7 MPa) after 1 year (Fig. 7). Fluids flowed vertically in the joint zones with a velocity of approximately 6.0×10^{-5} m/s. Fluids also flowed from the joint zones into adjacent wallrock and the flow velocity was 4.5×10^{-9} m/s at 5.4 km depth and 5.1×10^{-8} m/s at 4.6 km depth. The temperature in the profile at 5.4 km depth was higher than that at 4.6 km depth. The temperature in the wallrock adjacent to the joint zones reached 294 °C at 5.4 km depth and 230 °C at 4.6 km depth. The fluid density in the profile at 5.4 km depth varied between 799 and 1073 kg/m^3 and the fluid viscosity was between 1.3×10^{-4} and 4×10^{-4} Pa·s. For the joint zones, the Péclet number reached 7.9 in the profile at 5.4 km depth and 7.8 in the profile at 4.6 km depth. This indicates that the fluid flow in the joint zones were dominated by advection (Lester et al., 2012). In contrast, the Péclet number in the wallrock parts of the two profiles was much lower than 1, suggesting that the chemical reactions were dominated by reaction–diffusion processes (Lester et al., 2012).

The initial effective diffusion coefficients of silica D_e were equal in the two profiles because of the same initial viscosity and constant porosity. The D_e in the profile at 5.4 km depth increased to higher levels than that at 4.6 km depth after 1 year (Fig. 8). After 2 years, the D_e in the profile at 4.6 km depth increased but was still lower than that in the profile at 5.4 km depth.

5.2. Numerical experiment with variable viscosity and constant density

In the second numerical experiment, the fluid viscosity was as variable as in the first numerical experiment but the fluid density was fixed at 1073 kg/m^3. The constant density was the maximum in the first numerical experiment. The other parameters were the same as in the first numerical experiment.

The fluid pressure increased to 147.4–148.9 MPa in the profile at 5.4 km depth and 129.6–140.2 MPa in the profile at 4.6 km depth after 1 year (Fig. 9), which was lower than the corresponding pressure in the first numerical experiment. The fluid velocity in the joint zones was approximately 4.1×10^{-5} m/s, which was smaller than that in the first numerical experiment. The temperature in the wallrock adjacent to the joint zones reached 286 °C at 5.4 km depth and 192 °C at 4.6 km depth. Therefore, the heat transfer was slower than that in the first numerical experiment. The Péclet number was approximately 5.0 in the joint zones, which was lower than that in the first numerical experiment.

5.3. Numerical experiment with variable density and constant viscosity

In the third numerical experiment, the fluid density was as variable as in the first numerical experiment, but the fluid viscosity was fixed at 4×10^{-4} Pa·s. The fixed viscosity was the maximum in the first numerical experiment. The other parameters were the same as in the first numerical experiment.

The fluid pressure increased to 147.2–149.5 MPa in the profile at 5.4 km depth and 135.2–144.3 MPa in the profile at 4.6 km depth after 1 year (Fig. 10). Fluid flow in the joint zones had a velocity of

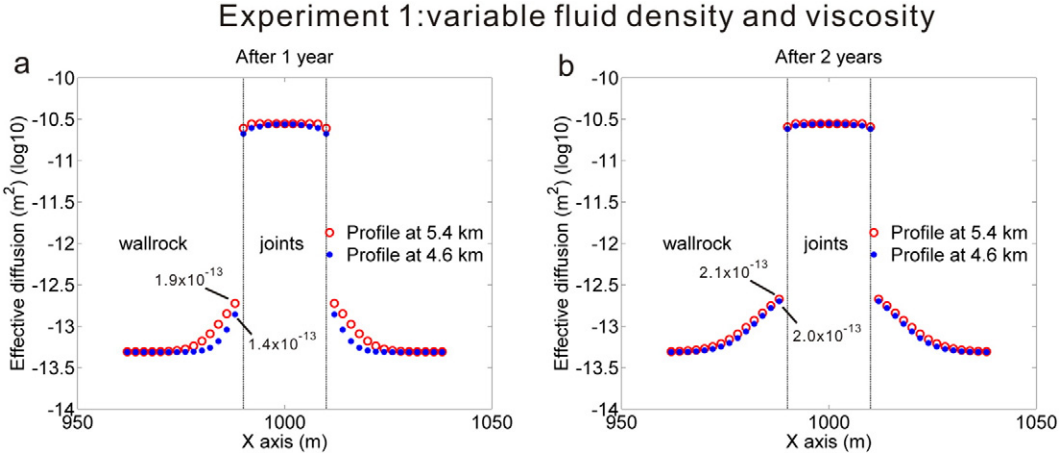

Fig. 8. The effective diffusion coefficients of silica in the first numerical experiment after 1 year (a) and 2 years (b). The coefficients have been logarithmically transferred.

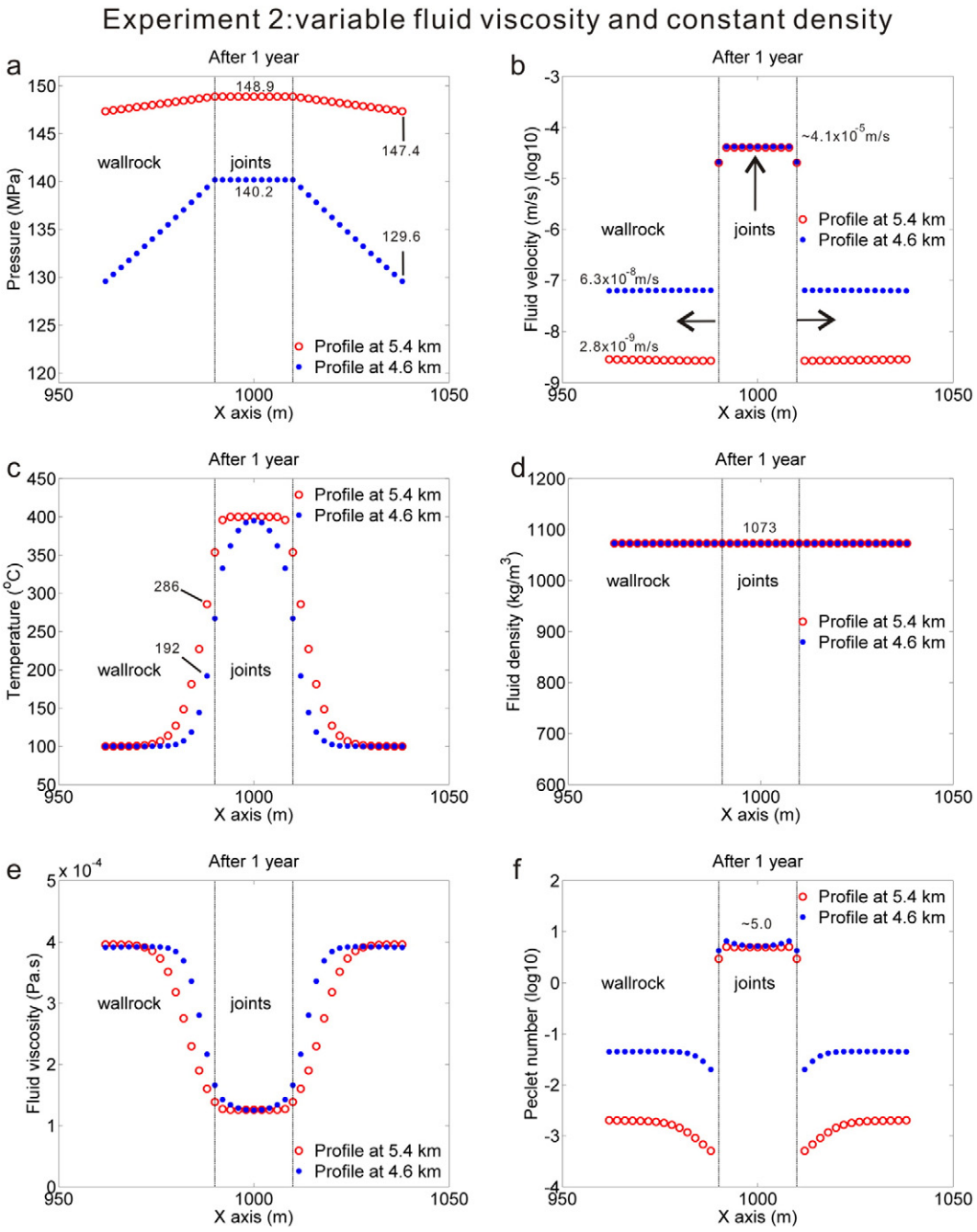

Fig. 9. The fluid flow and heat transfer in the second numerical experiment after 1 year: (a), (b), (c), (d), (e) and (f) are the fluid pressure, velocity, temperature, fluid density, fluid viscosity, and the Péclet number in the two profiles, respectively. The temperature and Péclet number have been logarithmically transferred.

1.2×10^{-5} m/s in the profile at 5.4 km depth and 2.0×10^{-5} m/s in the profile at 4.6 km depth, which was significantly slower than that in the first numerical experiment. The temperature of the profile at 5.4 km depth increased up to 242 °C, whereas the temperature in the profile at 4.6 km depth increased little compared to its initial values. Correspondingly, the profile at 5.4 km depth had different density and viscosity distributions from that at 4.6 km depth. The distribution of the Péclet number suggests that the fluid flow regime did not change compared that in the first numerical experiment.

5.4. Numerical experiment with depth-dependent permeability wallrock

In the fourth numerical experiment, the permeability and porosity of the wallrock Є2 were depth-dependent. The other parameters were the same to those in the first numerical experiment. The permeability of Є2 decreased from 10^{-16} to 10^{-17} m^2 downwards, and the corresponding porosity reduced from 1% to 0.46%. Thus, the wallrock was less permeable than that in the second numerical experiment. The permeability and porosity in the wallrock parts of profile at 5.4 km depth were $10^{-16.9}$ m^2 and 0.54%, respectively. The permeability and porosity in the wallrock parts of profile at 4.6 km depth were $10^{-16.4}$ m^2 and 0.75%, respectively.

The fluid pressure reached 147.3–149.2 MPa in the profile at 5.4 km depth and 134.6–142.8 MPa in the profile at 4.6 km depth (Fig. 11), which was slight lower than that in the first numerical experiment. The fluid flow from the joint zones to adjacent wallrock had a velocity of 2.7×10^{-9} m/s at 5.4 km depth and 3.4×10^{-8} m/s at 4.6 km depth, which was slower than that in the first numerical experiment.

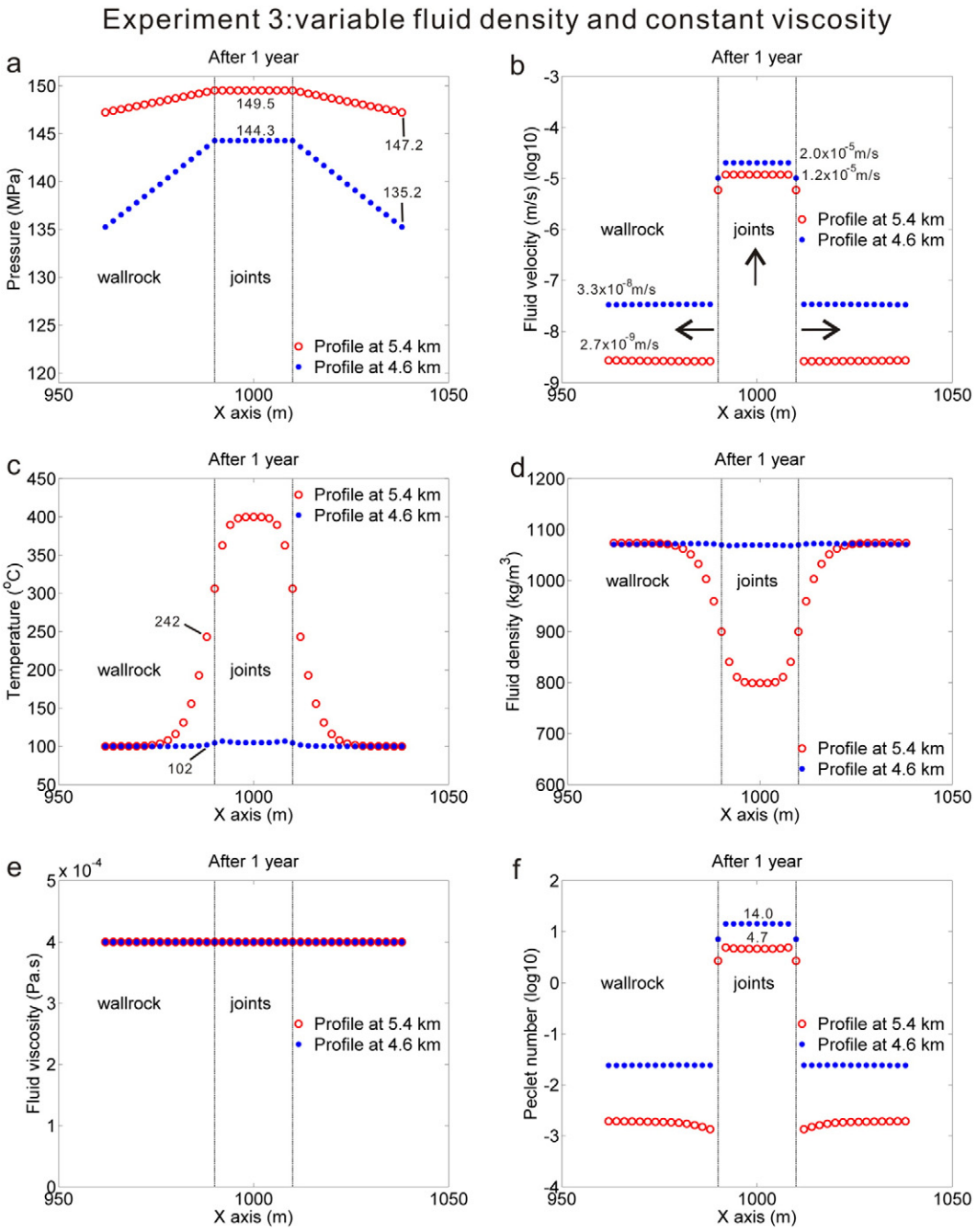

Fig. 10. The fluid flow and heat transfer in the third numerical experiment after 1 year: (a), (b), (c), (d), (e) and (f) are the fluid pressure, velocity, temperature, fluid density, fluid viscosity, and the Péclet number in the two profiles, respectively. The temperature and Péclet number have been logarithmically transferred.

The temperatures in the wallrock adjacent to the joint zones reached 294 °C at 5.4 km depth and 219 °C at 4.6 km depth. The Péclet number was approximately 8.0 in the joint zones and less than 1 in the wallrock, suggesting that the fluid regime did not change compared to the first numerical experiment.

The initial effective diffusion coefficients D_e of silica were 1.2×10^{-14} m^2/s and 2.7×10^{-14} m^2/s in the wallrock parts of profiles at 5.4 km depth and at 4.6 km depth, respectively. The D_e in the wallrock parts of the profile at 4.6 km depth increased to levels slightly higher than that at 5.4 km depth after 1 year (Fig. 12). The D_e in the wallrock adjacent to joint zones continued to increase after 2 years. The wallrock parts of the profile at 4.6 km depth had a maximum D_e of 1.1×10^{-13} m^2/s, whereas the maximum D_e in the wallrock parts of the deeper profile reached 5.4×10^{-14} m^2/s.

5.5. Numerical experiment with high-permeability joint zones

In the fifth numerical experiment, the permeability of the joint zones increased to 2×10^{-12} m^2 and its porosity increased to 12.6%. The other parameters were the same to those in the fourth numerical experiment.

The fluid pressure varied from 147.4 to 149.2 MPa in the profile at 5.4 km depth and from 135.4 to 142.9 MPa in the profile at 4.6 km depth, which was slight higher than that in the fourth numerical experiment (Fig. 13). The fluid velocity (1.2×10^{-4} m/s) in the joint zones

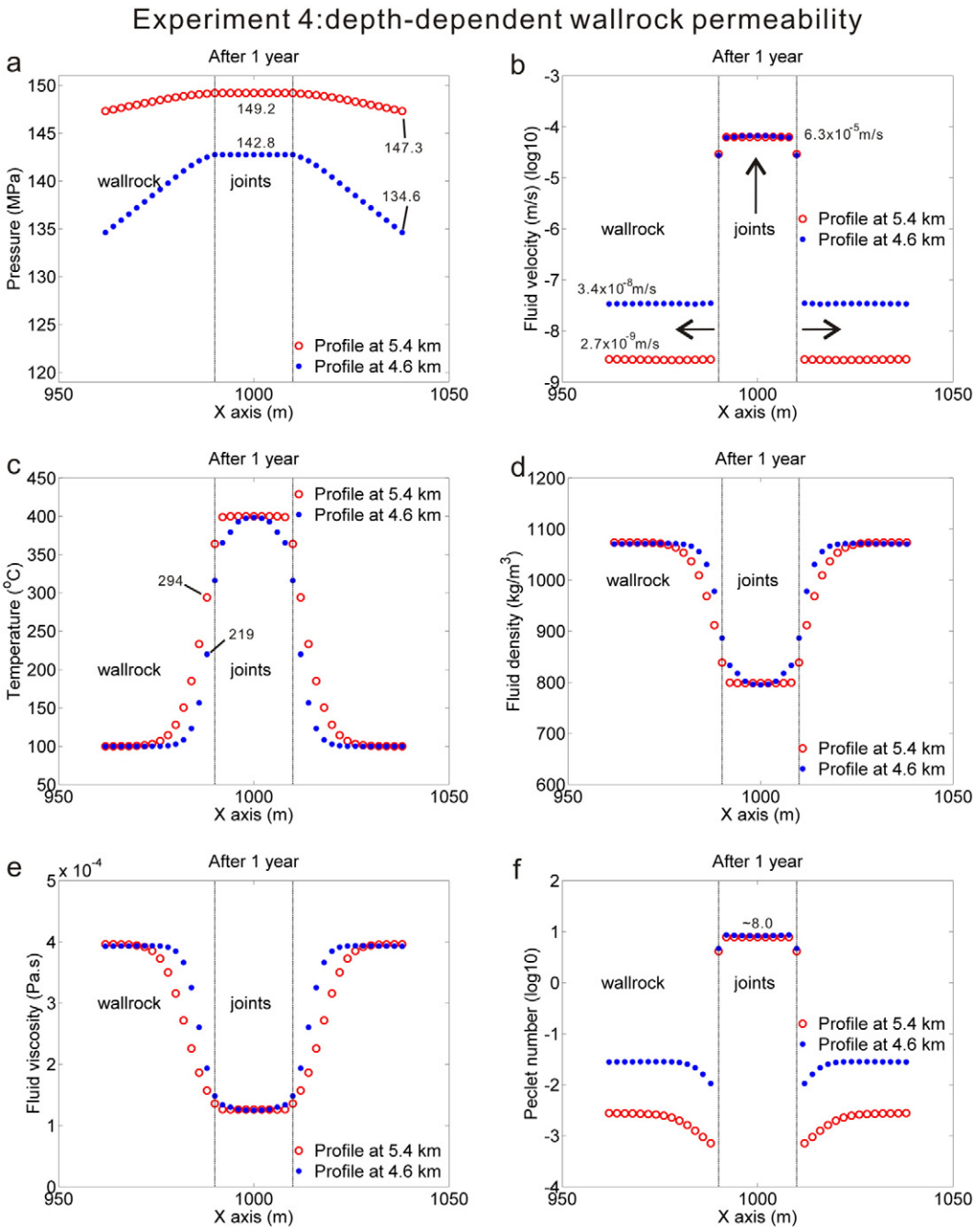

Fig. 11. The fluid flow and heat transfer in the fourth numerical experiment after 1 year: (a), (b), (c), (d), (e) and (f) are the fluid pressure, velocity, temperature, fluid density, fluid viscosity, and the Péclet number in the two profiles, respectively. The temperature and Péclet number have been logarithmically transferred.

was approximately two times that in the fourth numerical experiment (6.5×10^{-5} m/s). The wallrock adjacent to joint zones had a maximum temperature of 310 °C at 5.4 km depth and 290 °C at 4.6 km depth, which were higher than those in the first four numerical experiments. The Péclet number was approximately 14 in the joint zones, which was higher than that that in the fourth numerical experiment.

The wallrock parts of the profile at 4.6 km depth had higher effective diffusion coefficients D_e of silica than that at 5.4 km depth after 1 year. The D_e in the two profiles increased by a small amount after 2 years. The wallrock parts of the shallower profile reached a maximum D_e of 1.2×10^{-13} m^2/s, which was over two times the maximum (5.5×10^{-14} m^2/s) of the deeper profile (Fig. 14).

5.6. Numerical experiment with ladder-shaped joint zones

The joint zones were ladder-shaped in the sixth numerical experiment. The other parameters were the same as in the fifth numerical experiment. The width of the joint zones was 22 m in the profile at 5.4 km depth and 38 m in the profile at 4.6 km, which was wider than the width of the joint zones in previous numerical experiments. Red and blue dotted lines were used to show the boundary between the joint zones and adjacent wallrock in the profiles at 5.4 km depth and at 4.6 km depth, respectively.

The fluid pressure changed from 147.7 MPa to 148.9 MPa in the profile at 5.4 km depth and varied from 130.5 MPa to 142.0 MPa in

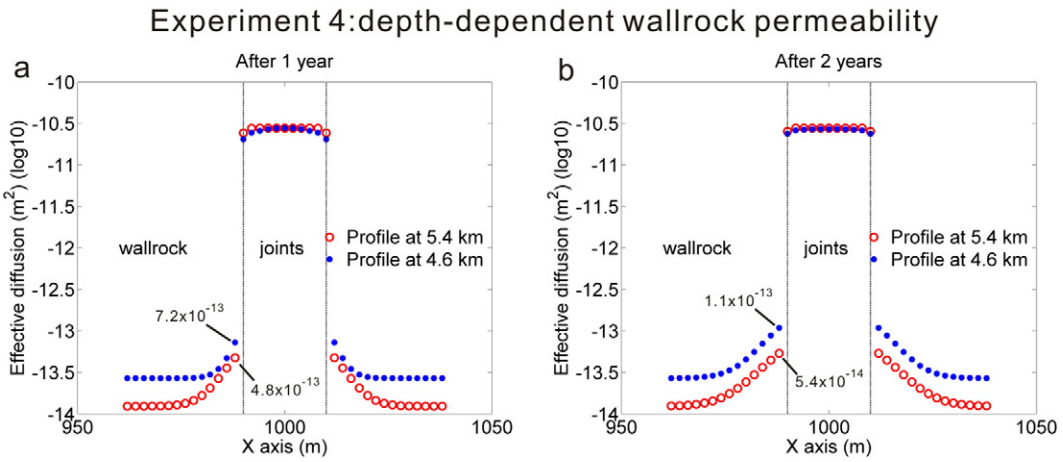

Fig. 12. The effective diffusion coefficients of silica in the fourth numerical experiment after 1 year (a) and 2 years (b). The coefficients have been logarithmically transferred.

the profile at 4.6 km depth after 1 year. The pressure levels of the profile at 4.6 km depth were lower than those in the fifth numerical experiment (Fig. 15). Fluid flow in the joint zones had a velocity of up to 4.2×10^{-5} m/s. The wallrock adjacent to joint zones had a temperature of 271 °C at 5.4 km depth and 109 °C at 4.6 km depth, which was significantly lower than that in the fifth numerical experiment. The Péclet number varied from 5 to 12 in the joint zones and was below 1 in the wallrock parts.

For the wallrock parts adjacent to joint zones, the effective diffusion coefficients D_e of silica in the profile at 5.4 km depth increased to higher levels than those at 4.6 km after 1 year (Fig. 16). The D_e of the profile at 4.6 km depth did not exceed that at 5.4 km depth until after 4 years. After 6 years, the D_e of the profile at 4.6 km depth reached a maximum of 8.2×10^{-14} m^2/s, whereas the maximum D_e at 5.4 km depth was 5.8×10^{-14} m^2/s.

6. Discussions

6.1. Influences of fluid density and viscosity on hydrothermal flow at Dajishan

The fluid density variation driven by a gradient in temperature or salinity is an effective mechanism to initiate and maintain free convection of basin brines and form hydrothermal deposits (e.g. Brown, 2014; Cui et al., 2012; Garven et al., 2001; Koziy et al., 2009; Raffensperger and Garven, 1995; Yang et al., 2004, 2006). However, the significance of the density-related gravity effect depends on the relative magnitude of the gravity-related versus the pressure-related flow components (Davies, 1987).

Fluid density in our first numerical experiment varied from 703 to 1074 kg/m^3 in the given temperature and pressure ranges. Note that the temperature and pressure ranges used in this paper are typical at the tungsten deposits in South China (Ni et al., 2015; Wang et al., 2011). The fluids had a gravity-driven gradient of 7–11 MPa/km, which accounted for at most 15% of the transient pressure gradient (73 MPa/m). Some fluid inclusions with a lower density (200–600 kg/m^3) have been found at other tungsten deposits in South China and Australia (e.g. Audétat et al., 2000; Wei et al., 2012). These low-density fluids have weaker gravity effect. The comparison between our first and second numerical experiments suggests that fluids with a larger density slowed fluid flow and heat transfer because gravity and the pressure gradient were in opposite directions. This is in contrast to the role of gravity in buoyancy-driven convection. Fluid density has a negative influence on the transient pressure-driven fluid flow at Dajishan. The significance of this negative influence depends on the relative magnitude of the gravity effect versus the pressure gradient.

Fluids with a higher viscosity flow slower (e.g. Hack et al., 2007; Thomas and Davidson, 2012). Fluid flow and heat transfer in our third numerical experiment was significantly slower than the first one because of having a higher viscosity. This is consistent with the traditional understanding. The fluid viscosity varied from 1×10^{-4} to 4×10^{-4} Pa·s in the temperature and pressure ranges at Dajishan. The variation of fluid viscosity was relatively wide compared to that of fluid density. Our first numerical experiment suggests that the viscosity change also has a major influence on the diffusion of silica from the joint zones to wallrock. Thus, fluid viscosity is a key parameter controlling formation of the alteration halos at Dajishan. Fluid viscosity is often fixed at a constant value in reactive transport models applied to the study of ore deposits (e.g. Aghbelagh and Yang, 2014; Cathles and Shannon, 2007; Geiger et al., 2002; He et al., 1999). However, our numerical experiments suggest that T–P–X dependent viscosity is important to capture the evolution of fluid-rock reactions.

Our current knowledge of viscosity of magmatic-hydrothermal fluids is limited compared to fluid density. Density of magmatic-hydrothermal fluids can be accurately calculated either by the equation of state or by formulated correlations (e.g. Driesner, 2007; Driesner and Heinrich, 2007; Gottschalk, 2007; Lewis and Lowell, 2009). However, experimental viscosity data and empirical formulas for brines at magmatic-hydrothermal transition are relatively lacking (Mao and Duan, 2009). Moreover, fluid-rich melt inclusions have been found in the quartz veins of the Xihuashan tungsten deposit and the stockscheider at the Dahutang tungsten deposit, South China (Gong et al., 2015; Huang et al., 2006). Viscosity of H_2O-bearing silicate melts decreases by 16 orders of magnitude when water concentration increases from 0 to 100% (Audétat and Keppler, 2004). The actual variation of fluid viscosity at Dajishan may be higher than that in our numerical experiments. Therefore, it is important to quantify viscosity of magmatic-hydrothermal fluids for deciphering the fluid-rock reactions at Dajishan and other magmatic-hydrothermal deposits further.

6.2. Implications for the alteration halos at Dajishan

The mechanisms forming the alteration halos at Dajishan are enigmatic for a few decades. Previous studies ascribed the alteration halos to magmatic-hydrothermal transitional fluids (Que and Xia, 1988), which is not supported by existing fluid inclusion studies (Ni et al., 2015; Wang et al., 2013a; Xi et al., 2008). Our numerical experiments provide some implications for formation of the alteration halos.

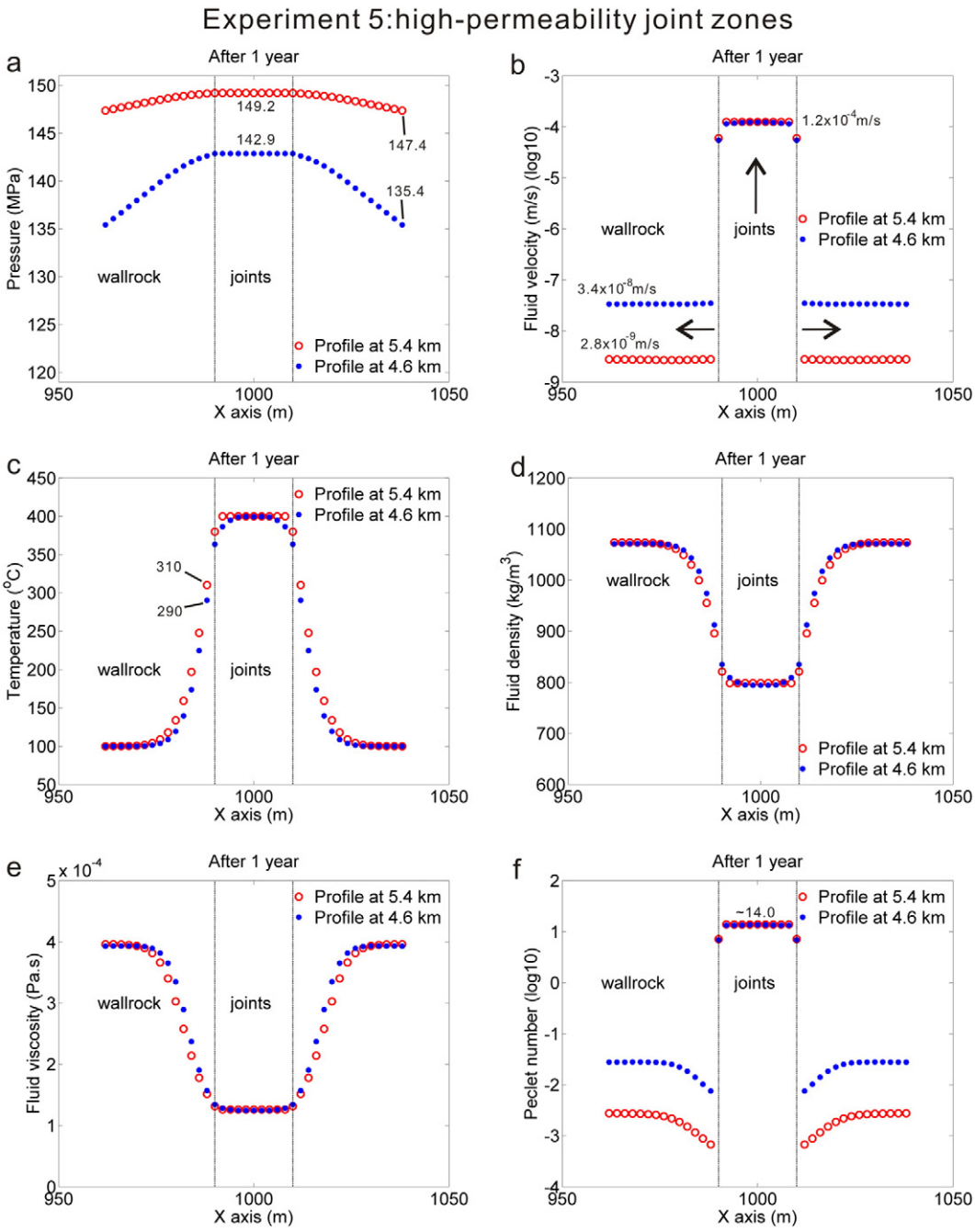

Fig. 13. The fluid flow and heat transfer in the fifth numerical experiment after 1 year: (a), (b), (c), (d), (e) and (f) are the fluid pressure, velocity, temperature, fluid density, fluid viscosity, and the Péclet number in the two profiles, respectively. The temperature and Péclet number have been logarithmically transferred.

The comparison of the alteration halo width at the two profiles was made based on Eq. (6). If G in Eq. (6) is assumed to be constant, the silification width normal to veins at Dajishan for a given time is positive correlated with the effective diffusion coefficient of silica D_e.

In our first numerical experiment, the wallrock adjacent to joint zones had a constant porosity and permeability. The fluid flow in the wallrock adjacent to joint zones was controlled by diffusion and chemical reactions were dominated by reaction–diffusion processes. The wallrock parts of the deeper profile had a higher D_e than that of the shallower profile because of having higher temperature. In this case, alteration halo width increases with increasing depth, which is inconsistent with the alteration characteristics at Dajishan.

In the fourth numerical experiment, wallrock porosity decreased with increasing depth. This counterbalanced the influence of temperature on the effective diffusion coefficient of silica because the effective diffusion coefficient was positive correlated with porosity squared. In this case, D_e decreased with increasing depth and it may form the alteration characteristics at Dajishan. Therefore, depth-dependent wallrock porosity and permeability are effective mechanisms forming the alteration halos at Dajishan.

Depth-dependent porosity is facilitated by the wallrock lithology at Dajishan. The wallrock at Dajishan is low-porosity metamorphosed sandstone, diorite, and granite. Laboratory experiments in the field of hydrogeology and rock engineering indicates that the porosity and

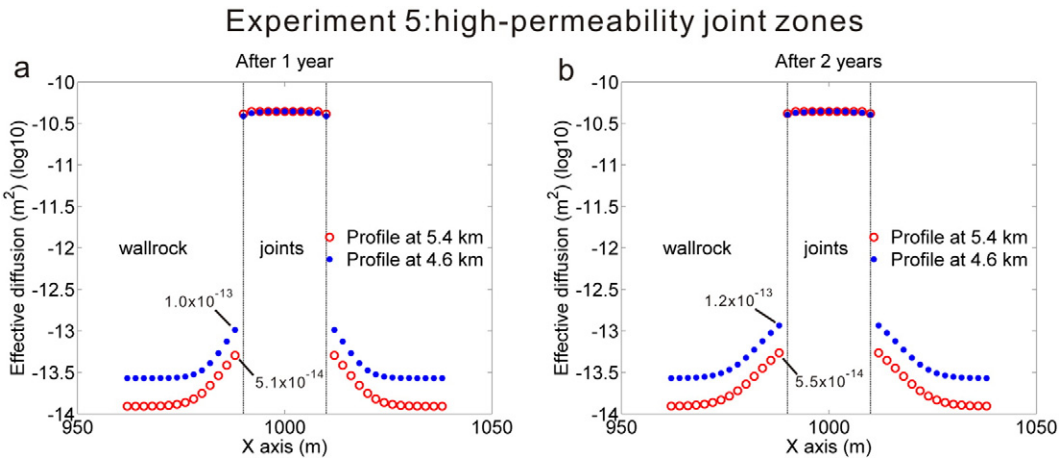

Fig. 14. The effective diffusion coefficients of silica in the fifth numerical experiment after 1 year (a) and 2 years (b). The coefficients have been logarithmically transferred.

permeability of low-porosity crystalline rocks decrease with increasing compressive stresses due to the closure of microcracks, but those of porous sedimentary rocks are insensitive to compaction (e.g. David et al., 1994; Heiland, 2003). Thus, the wallrock lithology at Dajishan favors formation of depth-dependent porosity and permeability. Also, joint density decreases downwards (Liu et al., 2014), suggesting that the wallrock are more intensively fractured at shallower levels than that at deeper levels. This is another reason why the porosity and permeability of wallrock are higher at shallower levels.

The hydraulic and geometric characteristics of joint zones also influence on the alteration halos at Dajishan. Our fifth numerical experiment suggests that an increase in joint zone permeability accelerated hydrothermal flow in joint zones and changed D_e in adjacent wallrock faster. High-permeability joint zones favor formation of thicker alteration halos at shallower levels. Vein systems at Dajishan are wedge-shaped. Our sixth numerical experiment indicates that an increase in joint zone width decelerated hydrothermal flow in joint zones and slowed the change D_e in adjacent wallrock. It should be noted that hydraulic and geometric characteristics of joint zones affect D_e only at the initial stages of hydrothermal fluids injected into joint zones, and species diffusion is finally controlled by the wallrock porosity.

6.3. Initial pressure and temperature conditions

Our models are across 1.6 km but have a constant initial temperature and pressure. The fluid pressure above the contact zone between the magma and wallrock may be at hydrostatic levels. In this case, the initial pressure at the bottom of our model reaches 55 MPa, which are higher than that in our models. It can be seen from Fig. 5 that this pressure deviation has a minor influence on fluid properties. However, an initial pressure of 55 MPa decreases the transient pressure gradient and increases the relative significance of the gravity effect compared to an initial pressure of 40 MPa. Therefore, an initial pressure of 40 MPa leads to skew results but does not change the conclusions in the previous section.

The initial temperature at deeper levels should be higher than those at shallower levels but the realistic temperature distribution before high-pressure fluids release is unknown. It can be seen from Fig. 5 that the initial temperature has an influence on initial fluid properties. This leads to some deviation from our numerical results. Because the fluid flow and heat transfer is mainly controlled by the high-pressure fluids and high-permeability joint zones, this deviation does not severely skew the results. Also, the initial diffusion coefficient D_s of silica at deeper levels may be higher than those at shallower levels. Because the effective diffusion coefficient D_e depends on D_s and porosity squared, the porosity distribution in vertical dimension is still the key variable controlling formation of the alteration halos at Dajishan. Treatment of a constant initial temperature indeed skews the results during the initial steps but does not affect the conclusion that depth-dependent wallrock porosity is one of the effective mechanisms forming the alteration halos at Dajishan.

6.4. Ore formation efficiency at Dajishan

The average WO_3 grade is 2.04% at Dajishan (Mao et al., 2013),which is 10^3 times the average concentration (5.87 ppm) of stream sediments in the Cathaysian Block and 10^4 times the Clarke value (0.6 ppm) for the crust in eastern China (Chi et al., 2012). It is important for the formation of an economic ore body to precipitate metals efficiently (Blundell et al., 2005; Heinrich et al., 2005; Henley and Berger, 2000; Polya, 1988). The Dajishan deposit should have efficient mechanisms to form the high grade of WO_3. Previous studies of fluid inclusions in wolframite suggest that wolframite deposition is attributed to a simple cooling process at Dajishan (Ni et al., 2015). Findings from the tungsten deposits elsewhere suggest that fluid–wallrock interactions decrease the efficiency of tungsten precipitation, therefore requiring more volumes of ore forming fluids (Heinrich, 1990; Heinrich et al., 1996; Polya, 1988). Our numerical experiments indicate that a rise of temperature increases the effective diffusion coefficients of chemical species in ore forming fluids, therefore accelerating the diffusion of metals from the joint zones to adjacent wallrock. This reduces the ore formation efficiency. However, this negative influence of temperature on ore formation efficiency is counterbalanced by depth-dependent permeability and porosity because the effective diffusion coefficients of chemical species are positive correlated with porosity squared. Low-porosity wallrock at deeper levels limits the fluid-wallrock interactions and improves the transport efficiency of tungsten from the fluid sources to precipitation sites, favoring formation of high-grade ores at Dajishan.

7. Conclusions

The mechanisms forming the alteration halos at Dajishan have been debated for a few decades. We investigate how variable fluid properties influence hydrothermal fluid flow and silica diffusion from fractures to adjacent wallrock using finite element based numerical experiments. The fluid density and viscosity are related to temperature and pressure

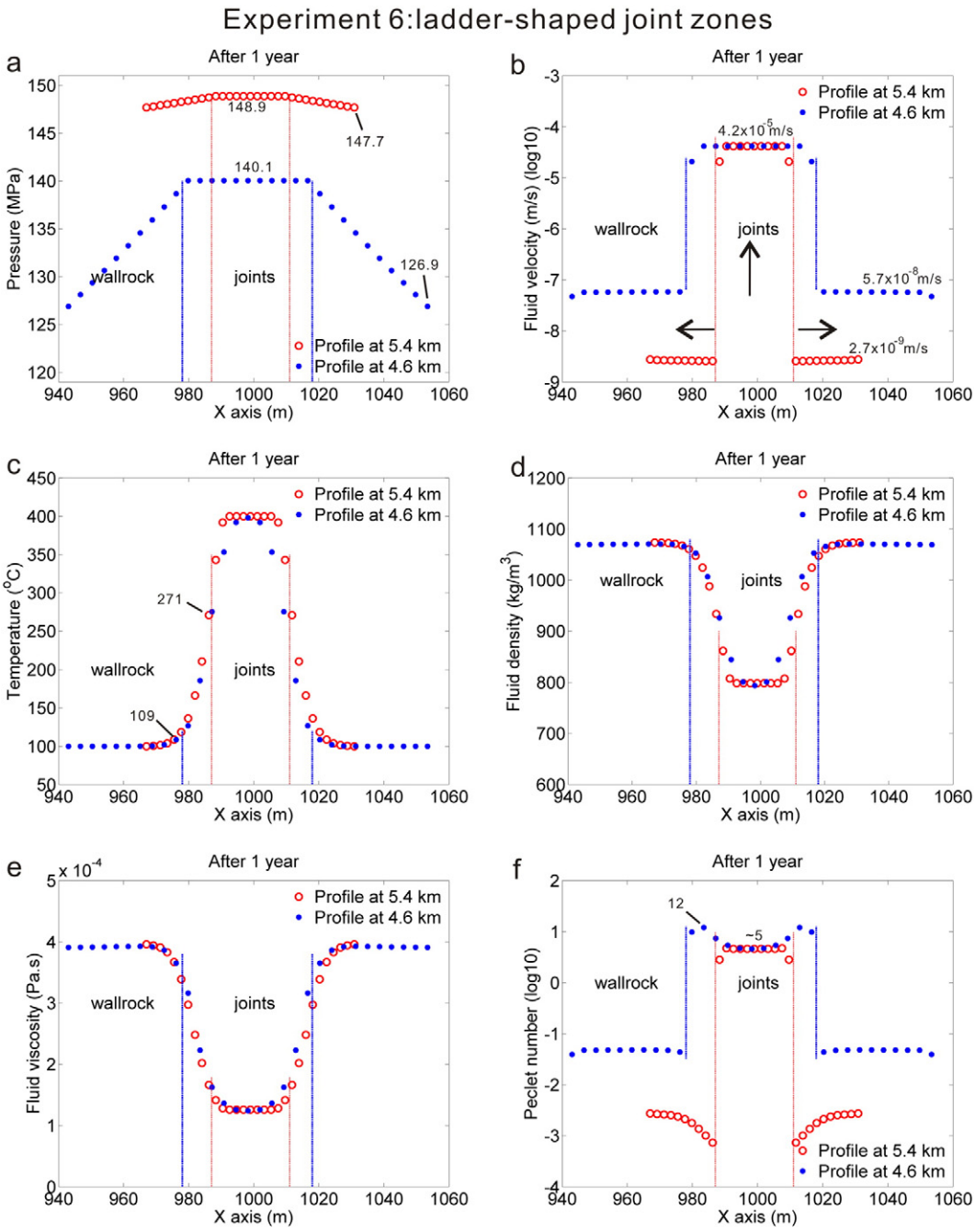

Fig. 15. The fluid flow and heat transfer in the sixth numerical experiment after 1 year: (a), (b), (c), (d), (e) and (f) are the fluid pressure, velocity, temperature, fluid density, fluid viscosity, and the Péclet number in the two profiles, respectively. Normal and bold dotted lines are the boundary between the joint zones and adjacent wallrock in the profiles at 5.4 km depth and at 4.6 km depth, respectively. The temperature and Péclet number have been logarithmically transferred.

in the numerical experiments. The effective diffusion coefficient of silica is dependent on temperature, fluid viscosity, and rock porosity. Although the hydrothermal fluid flow is non-reactive, our numerical experiments provide the following implications for transient thermal flow and formation of the alteration halos at Dajishan:

1. Fluid density exerts a negative influence on the transient pressure-driven fluid flow at Dajishan. Whether this negative influence is significant depends on the relative magnitude of the gravity effect versus the pressure gradient. This is different from the role of fluid density in some hydrothermal ore deposits controlled by free convection of basin brines.
2. Fluid viscosity varies greatly at the temperature and pressure ranges recorded by the fluid inclusions at Dajishan. Fluids with a higher viscosity flow slow. Variations of fluid viscosity also have a major influence on diffusion of silica from fractures to adjacent wallrock.
3. Constant-porosity wallrock forms alteration halos opposite to those at Dajishan. Depth-dependent wallrock porosity and permeability are effective mechanisms forming the alteration halos at Dajishan.
4. Hydraulic and geometric characteristics of joint zones affect the species diffusion at the initial stages of hydrothermal fluids injected into fractures. High-permeability narrow joint zones favors formation of thick alteration halos at shallower levels.
5. Depth-dependent wallrock porosity and permeability impede diffusion of metals from fractures to surrounding wallrock and increases ore formation efficiency at Dajishan.

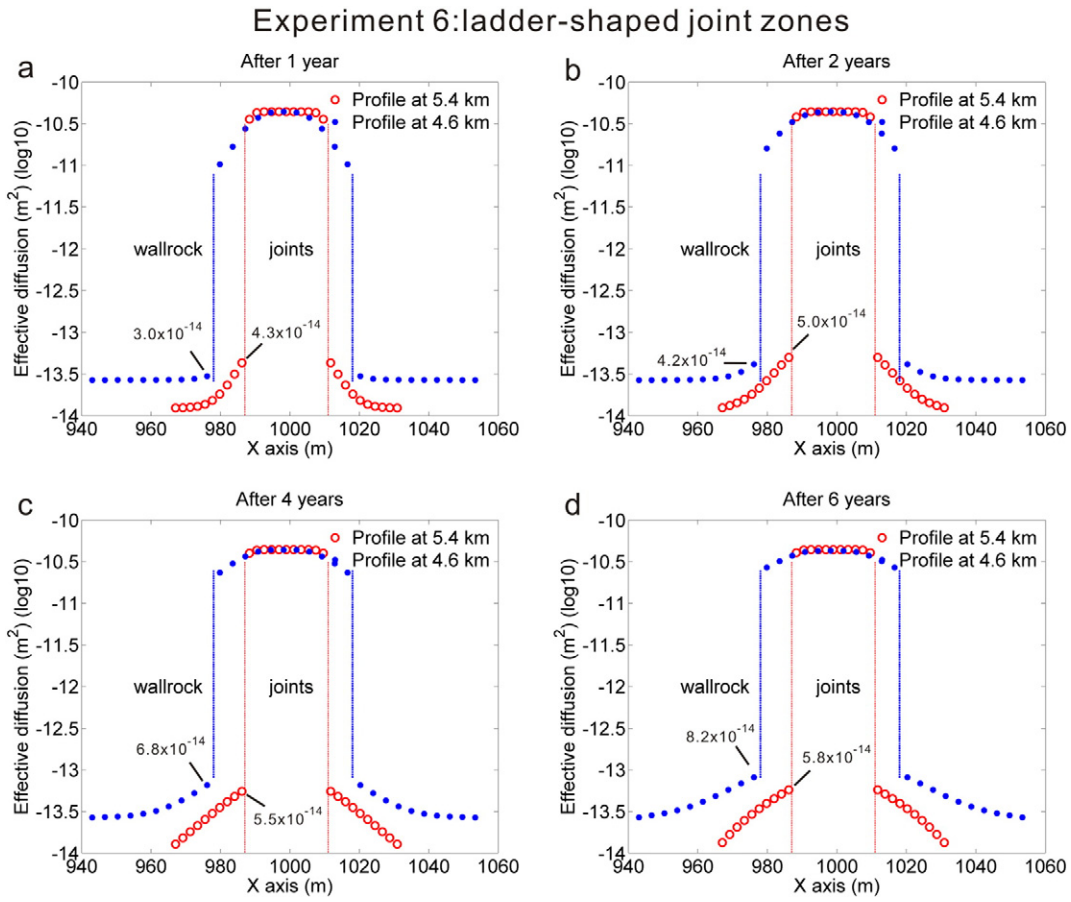

Fig. 16. The effective diffusion coefficients of silica in the sixth numerical experiment: (a) after 1 year; (b) after 2 years; (c) after 4 years; (d) after 6 years. Normal and bold dotted lines are the boundary between the joint zones and adjacent wallrock in the profiles at 5.4 km depth and at 4.6 km depth, respectively. The coefficients have been logarithmically transferred.

Acknowledgments

The work is financially supported by the NSFC grant (41373048), Australia Research Council (ARC DP 110103024), the MLR Nonprofit Industry Research Project (201411024), and the research project on "Mineral prediction by multisource geo-information in the Duolong mineral district" (12120115102301). The staff of Dajishan Tungsten Company is appreciated for their help in the field work. X.C Liu thanks Quanshu Li and Aleksandrov, A.A. for literature help. The numerical experiments were carried out by running the PANDAS software on the Savanna Supercomputer at The University of Queensland. The authors thank Peter Schaubs of CSIRO Earth Science and Resource Engineering and an anonymous reviewer for their constructive comments and suggestions that improve the original manuscript significantly.

Appendix A. Fluid density and viscosity models

Batzle and Wang (1992) present a function for brine density ρ by calculating the fresh water density ρ_w at a given temperature and pressure first and then adjusting ρ_w with the contribution of the dissolved solute ρ_s:

$$\rho = \rho_w + \rho_s. \quad (A-1)$$

Both ρ_w and ρ_s are polynomials of temperature, pressure, and salinity. Because the polynomials are very long, their expanded forms are not shown here.

Phillips et al. (1981) propose the following expression for viscosity of NaCl solutions:

$$\mu = \mu_w\left[1 + 0.0816m + 0.0122m^2 + 0.000128m^3 + 0.000629T\left(1 - e^{-0.7m}\right)\right] \quad (A-2)$$

where μ is the viscosity of NaCl solutions mPa·s, μ_w is the viscosity of water, m is the molality of NaCl in mol/kg, T is the temperature in °C. 1 Pa·s = 1000 mPa·s. Water viscosity is accurately described by the formulation of the International Association for the Properties of Water and Steam (Huber et al., 2009). However, this formulation is complicated and inconvenient for practical calculations. We used a simplified viscosity model for water developed by Mao and Duan (2009):

$$\ln\mu_w = \sum_{i=1}^{5} d_i T^{i-3} + \sum_{i=6}^{10} \rho_w d_i T^{i-8}. \quad (A-3)$$

The water density ρ_w can be obtained from Eq. (A-1). The ten constants d_i are listed in Mao and Duan (2009).

Appendix B. Rock compressibility and diffusion coefficients

The compressibility of rock matrix β_r is the reciprocal of its bulk modulus K (Zimmerman, 1990). Bulk modulus of rock matrix K is a function of Young's modulus E and Possion's ratio ν:

$$K = \frac{E}{3(1-2\nu)}. \quad (B-1)$$

Therefore,

$$\beta_r = \frac{3(1-2\nu)}{E}. \quad (B-2)$$

Zhou (2009) presents four groups of mechanical data of the metamorphosed sandstone at Dajishan. The four groups of data are 63,580 MPa (Young's modulus) and 0.1 (Poisson's ratio), 77,430 MPa and 0.174, 79,060 MPa and 0.141, 71,230 MPa and 0.139. The average compressibility of rock matrix is 2.8×10^{-11} Pa^{-1}.

Diffusion coefficient of chemical species in aqueous solutions D_s follows a function derived from the Stokes–Einstein equation:

$$\left(\frac{D_s\mu}{T}\right)_{T_1} = \left(\frac{D_s\mu}{T}\right)_{T_2} \quad (B-3)$$

where D_s and μ are the diffusion coefficient and fluid viscosity at a given temperature T, respectively (Li and Gregory, 1974; Simpson and Carr, 1958). The diffusion coefficient of dissolved silica in dilute aqueous solution is approximately 1.0×10^{-9} m^2/s at 25 °C (Applin, 1987; Rebreanu et al., 2008; Wollast and Garrels, 1971). This value was used as the reference diffusion coefficient in Eq. (B-3). The viscosity was calculated using the viscosity function of viscosity in Eq. (A-2).

References

Adams, J., Bachu, S., 2002. Equations of state for basin geofluids: algorithm review and intercomparison for brines. Geofluids 2 (4), 257–271.

Aghbelagh, Y.B., Yang, J., 2014. Effect of graphite zone in the formation of unconformity-related uranium deposits: Insights from reactive mass transport modeling. J. Geochem. Explor. 144 (Part A(0)), 12–27.

Applin, K.R., 1987. The diffusion of dissolved silica in dilute aqueous solution. Geochim. Cosmochim. Acta 51 (8), 2147–2151.

Audétat, A., Keppler, H., 2004. Viscosity of fluids in subduction zones. Science 303 (5657), 513–516.

Audétat, A., Gïther, D., Heinrich, C.A., 2000. Magmatic-hydrothermal evolution in a fractionating granite: a microchemical study of the Sn–W–F-mineralized mole granite (Australia). Geochim. Cosmochim. Acta 64 (19), 3373–3393.

Bachu, S., 1995. Flow of variable-density formation water in deep sloping aquifers: review of methods of representation with case studies. J. Hydrol. 164 (1), 19–38.

Batzle, M.L., Wang, Z., 1992. Seismic properties of pore fluids. Geophysics 57 (11), 1396–1408.

Blundell, D., Arndt, N., Cobbold, P.R., Heinrich, C., 2005. 9: processes of tectonism, magmatism and mineralization: lessons from Europe. Ore Geol. Rev. 27 (1–4), 333–349.

Bobertson, E.C., 1988. Thermal Properties of Rocks. The United States Geological Survey.

Boving, T.B., Grathwohl, P., 2001. Tracer diffusion coefficients in sedimentary rocks: correlation to porosity and hydraulic conductivity. J. Contam. Hydrol. 53 (1–2), 85–100.

Brown, A.C., 2014. Latent thermal effects from porcupine volcanics calderas underlying the white pine-presque isle stratiform copper mineralization, northern Michigan. Econ. Geol. 109 (7), 2035–2050.

Cann, J.R., McCaig, A.M., Yardley, B.W.D., 2015. Rapid generation of reaction permeability in the roots of black smoker systems, Troodos ophiolite, Cyprus. Geofluids 15 (1–2), 179–192.

Cao, X.F., et al., 2009. An infrared microscope investigation of fluid inclusions in coexisting quartz and wolframite: a case study of Yaogangxian quartz vein wolframite deposit. Mineral Deposits 28 (5), 611–620.

Cathles, L.M., Shannon, R., 2007. How potassium silicate alteration suggests the formation of porphyry ore deposits begins with the nearly explosive but barren expulsion of large volumes of magmatic water. Earth Planet. Sci. Lett. 262 (1–2), 92–108.

Chang, H., Wang, X., Wang, X., Liu, j., huang, H., 2006. The composition of melt inclusions in beryl from wolframite–quartz veins in Xihuashan, Jiangxi Province. Acta Petrol. Mineral. 26 (3), 259–268.

Chen, Y.C., Pei, R.F., Zhang, H.L., Lin, X.D., Li, C.Y., Hu, Y.J., Liu, H.Q., Xian, B.Q., 1989. The Geology of Nonferrous and Rare Metal Deposits Related to Mesozoic Granitoids in Nanling Region, China. Geological Publishing Housing, Beijing.

Chi, G.X., Xue, C.J., 2011. An overview of hydrodynamic studies of mineralization. Geosci. Front. 2 (3), 423–438.

Chi, Q.H., et al., 2012. Temporal and spatial distribution of tungsten and tin in South China Continent. Earth Sci. Front. 19 (3), 70–83 (In Chinese with English abstract).

Cox, S.F., Knackstedt, M.A., Braun, J., 2001. Principles of structural control on permeability and fluid flow in hydrothermal systems. Soc. Econ. Geol. Rev. 14, 1–24.

Cui, T., Yang, J., Samson, I.M., 2012. Solute transport across basement/cover interfaces by buoyancy-driven thermohaline convection: implications for the formation of unconformity-related uranium deposits. Am. J. Sci. 312 (9), 994–1027.

David, C., Wong, T.F., Zhu, W., Zhang, J., 1994. Laboratory measurement of compaction-induced permeability change in porous rocks: implications for the generation and maintenance of pore pressure excess in the crust. Pure Appl. Geophys. 143 (1–3), 425–456.

Davidson, P., Kamenetsky, V.S., 2001. Immiscibility and continuous felsic melt-fluid evolution within the Rio Blanco porphyry system, Chile: evidence from inclusions in magmatic quartz. Econ. Geol. 96 (8), 1921–1929.

Davies, P.B., 1987. Modeling areal, variable-density, ground-water flow using equivalent freshwater head—analysis of potentially significant errors. Proceedings of the Solving Ground Water Problems with Models, pp. 10–12.

Driesner, T., 2007. The system H_2O–NaCl. Part II: correlations for molar volume, enthalpy, and isobaric heat capacity from 0 to 1000 °C, 1 to 5000 bar, and 0 to 1 X_{NaCl}. Geochim. Cosmochim. Acta 71 (20), 4902–4919.

Driesner, T., Heinrich, C.A., 2007. The system H_2O–NaCl. Part I: correlation formulae for phase relations in temperature–pressure–composition space from 0 to 1000 °C, 0 to 5000 bar, and 0 to 1 X_{NaCl}. Geochim. Cosmochim. Acta 71 (20), 4880–4901.

Fournier, R.O., 1999. Hydrothermal processes related to movement of fluid from plastic into brittle rock in the magmatic-epithermal environment. Econ. Geol. 94 (8), 1193–1212.

Garven, G., Bull, S., Large, R., 2001. Hydrothermal fluid flow models of stratiform ore genesis in the McArthur Basin, Northern Territory, Australia. Geofluids 1 (4), 289–311.

Geiger, S., Haggerty, R., Dilles, J.H., Reed, M.H., Matthäi, S.K., 2002. New insights from reactive transport modelling: the formation of the sericitic vein envelopes during early hydrothermal alteration at Butte, Montana. Geofluids 2 (3), 185–201.

Gerdes, M.L., Baumgartner, L.P., Person, M., 1998. Convective fluid flow through heterogeneous country rocks during contact metamorphism. J. Geophys. Res. Solid Earth 103 (B10), 23983–24003.

Gong, X., et al., 2015. A study of ore-forming fluids in the Shimensi tungsten deposit, Dahutang tungsten polymetallic ore field, Jiangxi Province, China. Acta Geol. Sin. 89 (3), 822–835.

Gottschalk, M., 2007. Equations of state for complex fluids. Rev. Mineral. Geochem. 65 (1), 49–97.

Hack, A.C., Thompson, A.B., Aerts, M., 2007. Phase relations involving hydrous silicate melts, aqueous fluids, and minerals. Rev. Mineral. Geochem. 65 (1), 129–185.

Hanson, R.B., 1995. The hydrodynamics of contact metamorphism. Geol. Soc. Am. Bull. 107 (5), 595–611.

Hayba, D.O., Ingebritsen, S.E., 1997. Multiphase groundwater flow near cooling plutons. J. Geophys. Res. 102 (B6), 12235–12252.

He, W., Zhengyu, B., Tieping, L., 1999. One-dimensional reactive transport models of alteration in the Tongchang porphyry copper deposit, Dexing District, Jiangxi Province, China. Econ. Geol. 94 (3), 307–323.

Heiland, J., 2003. Laboratory testing of coupled hydro-mechanical processes during rock deformation. Hydrogeol. J. 11 (1), 122–141.

Heinrich, C.A., 1990. The chemistry of hydrothermal tin(-tungsten) ore deposition. Econ. Geol. 85 (3), 457–481.

Heinrich, C.A., Halter, W., Landtwing, M.R., Pettke, T., 2005. The formation of economic porphyry copper (-gold) deposits: constraints from microanalysis of fluid and melt inclusions. Geol. Soc. Lond., Spec. Publ. 248 (1), 247–263.

Heinrich, C.A., Walshe, J.L., Harrold, B.P., 1996. Chemical mass transfer modelling of ore-forming hydrothermal systems: current practise and problems. Ore Geol. Rev. 10 (3–6), 319–338.

Henley, R.W., Berger, B.R., 2000. Self-ordering and complexity in epizonal mineral deposits. Annu. Rev. Earth Planet. Sci. 28, 669–719.

Hu, R.-Z., et al., 2012. Mantle-derived noble gases in ore-forming fluids of the granite-related Yaogangxian tungsten deposit, Southeastern China. Mineral. Deposita 47 (6), 623–632.

Huang, H., Chang, H., Fu, J., Wang, X., Li, T., 2006. Formation pressure of wolframite_vein deposits and emplacement depth of related granite in Xihuashan, Jiangxi Province. Mineral Deposits 25 (5), 562–571 (In Chinese with English Abstract).

Hubbert, M.K., 1953. Entrapment of petroleum under hydrodynamic conditions. AAPG Bull. 37 (8), 1954–2026.

Huber, M.L., Perkins, R.A., Laesecke, A., Friend, D.G., Sengers, J.V., 2009. New international formulation for the viscosity of H_2O. J. Phys. Chem. Ref. Data 38 (2), 101–125.

Ingebritsen, S.E., Appold, M.S., 2012. The physical hydrogeology of ore deposits. Econ. Geol. 107, 559–584.

Ingebritsen, S.E., Manning, C.E., 2010. Permeability of the continental crust: dynamic variations inferred from seismicity and metamorphism. Geofluids 10, 193–205.

Ingebritsen, S.E., Geiger, S., Hurwitz, S., Driesner, T., 2010. Numerical simulation of magmatic hydrothermal systems. Rev. Geophys. 48 (1), 1–33.

Jiang, G.H., Hu, R.Z., Xie, G.Q., Zhao, J.H., Tang, Q.L., 2004. K–Ar ages of plutonism and mineralization at the Dajishan tungsten deposit, Jiangxi Province, China. Acta Mineral. Sin. 24 (3), 253–256 (In Chinese with English abstract).

Kamenetsky, V.S., Wolfe, R.C., Eggins, S.M., Mernagh, T.P., Bastrakov, E., 1999. Volatile exsolution at the Dinkidi Cu–Au porphyry deposit, Philippines: a melt-inclusion record of the initial ore-forming process. Geology 27 (8), 691–694.

Koziy, L., Bull, S., Large, R., Selley, D., 2009. Salt as a fluid driver, and basement as a metal source, for stratiform sediment-hosted copper deposits. Geology 37 (12), 1107–1110.

Lester, D.R., Ord, A., Hobbs, B.E., 2012. The mechanics of hydrothermal systems: II. Fluid mixing and chemical reactions. Ore Geol. Rev. 49 (0), 45–71.

Lewis, K.C., Lowell, R.P., 2009. Numerical modeling of two-phase flow in the NaCl–H_2O system: introduction of a numerical method and benchmarking. J. Geophys. Res. Solid Earth 114 (B5), B05202.

Li, Y., Gregory, S., 1974. Diffusion of ions in sea water and in deep-sea sediments. Geochim. Cosmochim. Acta 38 (5), 703–714.

Li, Q., Xing, H., 2015. Numerical analysis of the material parameter effects on the initiation of hydraulic fracture in a near wellbore region. J. Nat. Gas Sci. Eng. 27, 1597–1608. http://dx.doi.org/10.1016/j.jngse.2015.10.023.

Lin, X., Zhang, D., Zhang, C., 1986. A discussion on the property of ore-forming fluid of the wolframite quartz-vein in the Yaogangxian tungsten deposit, Yizhang County, Hunan Province. J. Earth Sci. 11 (2), 153–160.

Liu, Y.J., Ma, D.S., 1993. Vein-type tungsten deposits of China and adjoining regions. Ore Geol. Rev. 8, 233–246.
Liu, J., Mao, J., Ye, H., Zhang, W., 2011. Geology, geochemistry and age of the Hukeng tungsten deposit, southern China. Ore Geol. Rev. 43 (1), 50–61.
Liu, X., Xing, H., Zhang, D., 2014. Fluid focusing and its link to vertical morphological zonation at the Dajishan vein-type tungsten deposit, South China. Ore Geol. Rev. 62 (1), 245–258.
London, D., 2014. A petrologic assessment of internal zonation in granitic pegmatites. Lithos 184, 74–104.
Lu, H., Shih, J., Yu, C., 1974. Determination of the temperature of ore formation and diagenesis of a deposit from Southern China. Geochimica 3, 145–156.
Ma, X., Chen, W., 1984. Expenrimental studies of mineral inclusions from the Dajishan quartz-vein type tungsten deposit with an approach to ore genesis. Bull. Inst. Mineral Deposits 1, 57–69.
Mao, S., Duan, Z., 2009. The viscosity of aqueous alkali-chloride solutions up to 623 K, 1,000 bar, and high ionic strength. Int. J. Thermophys. 30 (5), 1510–1523.
Mao, J., Yanbo, C., Maohong, C., Pirajno, F., 2013. Major types and time–space distribution of Mesozoic ore deposits in South China and their geodynamic settings. Mineral. Deposita 48 (3), 267–294.
Ni, P., et al., 2015. An infrared microthermometric study of fluid inclusions in coexisting quartz and wolframite from Late Mesozoic tungsten deposits in the Gannan metallogenic belt, South China. Ore Geol. Rev. 65Part 4 (0), 1062–1077.
Oda, M., 1985. Permeablity tensor for discontinuous rock masses. Géotechnique 35 (4), 483–495.
Pepinov, R.I., Yusufova, V.D., Lobkova, N.V., 1977. Experimental investigation of viscosity of aqueous-solutions of NaCl at high-temperatures and pressures. Therm. Eng. 24 (9), 40–43.
Phillips, O.M., 1991. Flow and Reactions in Permeable Rocks. Cambridge University Press (295 pp.).
Phillips, S.L., Igbene, A., Fair, J.A., Ozbek, H., Tavana, M., 1981. A Technical Databook for Geothermal Energy Utilization.
Polya, D.A., 1988. Efficiency of hydrothermal ore formation and the Panasqueira W–Cu(Ag)–Sn vein deposit. Nature 333 (6176), 838–841.
Qiu, J., McInnes, B.I.A., Xu, X., Allen, C.M., 2004. Zircon ELA-ICP_MS dating for Wuliting pluton at Dajishan, Southern Jiangxi and new recognition about its relation to tungsten mineralization. Geol. Rev. 50 (2), 125–133.
Que, M.D., Xia, W.H., 1988. The property and mechanism of the mineralization concentration in Dajishan tungsten deposit, Jiangxi Province. Earth Sci. 13 (2), 177–185.
Raffensperger, J.P., Garven, G., 1995. The formation of unconformity-type uranium ore deposits; 1, coupled groundwater flow and heat transport modeling. Am. J. Sci. 295 (5), 581–636.
Rebreanu, L., Vanderborght, J.-P., Chou, L., 2008. The diffusion coefficient of dissolved silica revisited. Mar. Chem. 112 (3), 230–233.
Rogers, P.S.Z., Pitzer, K.S., 1982. Volumetric properties of aqueous sodium chloride solutions. J. Phys. Chem. Ref. Data 11 (1), 15–81.
Rutqvist, J., 2015. Fractured rock stress-permeability relationships from in situ data and effects of temperature and chemical–mechanical couplings. Geofluids 15 (1–2), 48–66.
Semenyuk, E., Zarembo, V., Feodorov, M., 1977. Experimental apparatus for the measurements of viscosity of aqueous solutions at temperatures 273-673 K and at pressures up to 200 MPa. Russ. J. Phys. Chem. 50, 315–319.
Simpson, J.H., Carr, H.Y., 1958. Diffusion and nuclear spin relaxation in water. Phys. Rev. 111 (5), 1201–1202.
Snow, D.T., 1969. Anisotropie permeability of fractured media. Water Resour. Res. 5 (6), 1273–1289.
Steefel, C.I., Lichtner, P.C., 1998. Multicomponent reactive transport in discrete fractures: I. Controls on reaction front geometry. J. Hydrol. 209 (1–4), 186–199.
Stober, I., Bucher, K., 2015. Hydraulic conductivity of fractured upper crust: insights from hydraulic tests in boreholes and fluid–rock interaction in crystalline basement rocks. Geofluids 15 (1–2), 161–178.
Sun, G.A., 1989. Dajishan tungsten, niobium, and tantalum deposit in Jiangxi Province. In: Chen, Y.C., et al. (Eds.), The Geology of Nonferrous and Rare Metal Deposits Related to Mesozoic Granitoids in Nanling Region. Geological Publishing Housing, Beijing, pp. 74–87.
Thomas, R., Davidson, P., 2012. Water in granite and pegmatite-forming melts. Ore Geol. Rev. 46, 32–46.
Thomas, R., Webster, J.D., Heinrich, W., 2000. Melt inclusions in pegmatite quartz: complete miscibility between silicate melts and hydrous fluids at low pressure. Contrib. Mineral. Petrol. 139 (4), 394–401.
Van Loon, L.R., Mibus, J., 2015. A modified version of Archie's law to estimate effective diffusion coefficients of radionuclides in argillaceous rocks and its application in safety analysis studies. Appl. Geochem. 59, 85–94.
Veksler, I.V., 2004. Liquid immiscibility and its role at the magmatic–hydrothermal transition: a summary of experimental studies. Chem. Geol. 210 (1–4), 7–31.
Walder, J., Nur, A., 1984. Porosity reduction and crustal pore pressure development. J. Geophys. Res. Solid Earth 89 (B13), 11539–11548.
Wang, D., Lu, H., Bi, X., 2011. Comparison of characteristics of ore forming fluids between quartz-vein tungsten deposits and porphyry copper deposits associated with granitic rocks. Earth Sci. Front. 18 (5), 121–131 (In Chinese with English Abstract).
Wang, X.D., Ni, P., Yuan, S.D., Wu, S.H., 2013a. Fluid inclusion studies of Dajishan tungsten deposit in Jiangxi Province. Mineral Deposits 32, 308–322.
Wang, X.D., Ni, P., Yuan, S.D., Wu, S.H., 2013b. Fluid inclusion studies on coexisting cassiterite and quartz from the Piaotang tungsten deposit, Jiangxi Province, China. Acta Geol. Sin. 87 (6), 850–859.
Wang, R.C., et al., 2003. Accessory minerals in the Xihuashan Y-enriched granitic complex, southern China: a record of magmatic and hydrothermal stages of evolution. Can. Mineral. 41 (3), 727–748.
Wei, W.F., Hu, R.Z., Bi, X.W., Peng, J.T., Su, W.C., Song, S.Q., Shi, S.H., 2012. Infrared microthermometric and stable isotopic study of fluid inclusions in wolframite at the Xihuashan tungsten deposit, Jiangxi province, China. Mineral. Deposita 47 (6), 589–605.
Weis, P., 2015. The dynamic interplay between saline fluid flow and rock permeability in magmatic-hydrothermal systems. Geofluids 15 (1–2), 350–371.
Wollast, R., Garrels, R.M., 1971. Diffusion coefficient of silica in seawater. Nature 229 (3), 94.
Xi, B.B., Zhang, D.H., Zhou, L.M., Zhang, W.H., Wang, C., 2008. Characteristics of ore-forming fluid evolution in Dajishan tungsten deposit, Quannan County, Jiangxi. Acta Geograph. Sin. 82 (7), 956–966.
Xing, H., 2014. Finite element simulation of transient geothermal flow in extremely heterogeneous fractured porous media. J. Geochem. Explor. 144, 168–178.
Xing, H.L., Makinouchi, A., 2002. Three dimensional finite element modeling of thermomechanical frictional contact between finite deformation bodies using R-minimum strategy. Comput. Methods Appl. Mech. Eng. 191 (37–38), 4193–4214.
Xing, H., Liu, Y., Gao, J., Chen, S., 2015. Recent development in numerical simulation of enhanced geothermal reservoirs. J. Earth Sci. 26 (1), 28–36.
Xing, H.L., Makinouchi, A., Mora, P., 2007. Finite element modeling of interacting fault systems. Phys. Earth Planet. Inter. 163 (1–4), 106–121.
Yang, J., Bull, S., Large, R., 2004. Numerical investigation of salinity in controlling ore-forming fluid transport in sedimentary basins: example of the HYC deposit, Northern Australia. Mineral. Deposita 39 (5–6), 622–631.
Yang, M.G., Huang, S.B., Lou, F.S., Tang, W.X., Mao, S.B., 2009. Lithospheric structure and large-scale metallogenic processes in southeast China. Chin. Geol. 36 (3), 528–545.
Yang, J., Large, R.R., Bull, S., 2006. Basin-scale numerical modeling to test the role of buoyancy-driven fluid flow and heat transfer in the formation of stratiform Zn–Pb–Ag deposits in the Northern Mount Isa Basin. Econ. Geol. 101, 1275–1292.
Yang, J.h., et al., 2013. Garnet geochemistry of tungsten-mineralized Xihuashan granites in South China. Lithos 177 (0), 79–90.
Zhang, D., 1987. A further discussion on the property of ore-forming fluid of the quartz-vein type wolframite deposit. J. Earth Sci. 12 (2), 185–192.
Zhang, W.L., Hua, R.M., Wang, R.C., Chen, P.R., Li, H.M., 2006. New dating of the Dajishan granite and related tungsten mineralization in South Jiangxi. Acta Geol. Sin. 80 (7), 956–962 (In Chinese with English abstract).
Zhang, W.L., Hua, R.M., Wang, R.C., Li, H.M., Chen, P.R., 2004. Single zircon U–Pb isotopic age of the Wuliting granite in Dajishan area of Jiangxi, and its geological implication. Acta Geol. Sin. 78 (3), 352–358 (In Chinese with English abstract).
Zhang, G.X., Xie, Y.N., Yu, F.J., Zhang, H.B., 1997. Stable isotope geochemistry of distinct metallogenic stages of tungsten deposits in Dajishan mine, Jiangxi. Acta Geosci. Sin. 18, 197–199 (In Chinese with English abstract).
Zhang, S.M., et al., 2011. Re–Os isotopic dating of molybdenite from Dajishan tungsten deposit in Jiangxi Province. Mineral Deposits 30 (6), 1113–1121 (In Chinese with English abstract).
Zhou, L.M., 2009. Numerical Modeling of Paleo-tectonic Stress Field and Metallogenic Prognosis in Dajishan Tungsten Deposit, Quannan, Jiangxi Published M.Sc. Thesis Thesis China University of Geosciences (Beijing), Beijing, China (67 pp.).
Zhou, X.M., Sun, T., Shen, W.Z., Shu, L.S., Niu, Y.L., 2006. Petrogenesis of Mesozoic granitoids and volcanic rocks in south China: a response to tectonic evolution. Episodes 29 (1), 26–33.
Zhu, Y.L., Li, C.Y., Lin, Y.H., 1981. Tungsten Deposit Geology in South Jiangxi Province. Jiangxi People's Publishing House, Nanchang.
Zhu, X., Wang, J., Wang, Y., Chen, X., Fu, Q., 2014. Relatively closed ore-forming systems in the tungsten-bearing vein: a case study of the Yaogangxian deposit, Hunan Province. Acta Geol. Sin. 88 (5), 825–835.
Zhuang, L.C., Lin, W.S., Xie, T.H., 1991. Stable isotope geochemistry of the Dajishan tungsten mine in Jiangxi Province. Bull. Yichang Inst. Geol. Miner. Res. 16, 109–120.
Zimmerman, R.W., 1990. Compressibility of Sandstones. Elsevier, New York (173 pp.).